Thin–Walled Structures 231 (2026) 115553

Contents lists available at ScienceDirect

Thin-Walled Structures

journal homepage: www.elsevier.com/locate/tws

Full length article

Free vibration analysis of variable-stiffness composite cylindrical panels with complex cutout geometries

A. Milazzo

Department of Engineering, University of Palermo, Viale delle Scienze, Bldg 8, 90128 Palermo, Italy

ARTICLE INFO

Keywords:
Free vibration
Variable-stiffness composites
Cylindrical panels
Cutout geometries
Fibre steering
Level-set method

ABSTRACT

A unified computational framework for the free vibration analysis of variable-stiffness composite laminated cylindrical panels with complex cutout geometries, non-uniform thickness distributions, and multi-region laminates is presented. Based on first-order shear deformation theory, the framework enables the single-domain analysis of cylindrical panels containing multiple cutouts of arbitrary shape, without introducing independent subdomain fields or interface continuity constraints. Geometric complexity is handled through implicit level-set descriptions combined with high-order quadrature schemes, enabling accurate numerical integration over irregular domains. The accuracy of the framework is assessed through comparisons with high-fidelity finite element solutions, showing very good agreement with reference solutions across a range of benchmark configurations. Representative applications demonstrate its capability to analyse cylindrical panels with complex stiffness distributions and geometric discontinuities, and to investigate the influence of stiffness variability and cutout geometry on the dynamic response. For the configurations examined, the results show that stiffness tailoring through spatially varying fibre orientations enables mode-dependent tailoring of the natural frequencies of cylindrical panels with cutouts. Overall, the proposed framework provides an accurate and versatile tool for the vibration analysis of composite cylindrical panels with variable stiffness and complex cutout geometries, and establishes a sound basis for future developments in the design, optimization, and performance tailoring of advanced lightweight structures.

1. Introduction

Composite laminated cylindrical shells and panels are extensively employed in aerospace, marine, automotive, and energy engineering because of their outstanding stiffness-to-weight and strength-to-weight ratios. Typical applications include aircraft fuselage sections, launch vehicle fairings, satellite structures, pressure vessels, and wind turbine components, where lightweight design and high structural efficiency are primary requirements. Since these structures are frequently subjected to dynamic loading during service, accurate prediction of their vibration characteristics is essential to prevent resonance, ensure structural integrity, improve fatigue resistance, and guarantee reliable long-term performance. Recent advances in automated fibre placement (AFP) and related manufacturing technologies have enabled the fabrication of variable-stiffness (VS) composite laminates, in which the fibre orientation varies continuously along curvilinear paths [1,2]. Compared with conventional straight-fibre laminates, VS configurations offer substantially greater design flexibility by enabling stiffness tailoring to enhance buckling resistance, redistribute stresses, and tailor the dynamic response [3]. These capabilities are particularly attractive for cylindrical shell structures containing cutouts, which are commonly introduced in practical applications to accommodate inspection and maintenance access, windows, doors, weight reduction, or the integration of onboard systems. Although functionally necessary, such geometric discontinuities introduce local stiffness reductions, stress concentrations, and modal distortions that may significantly affect the vibration behaviour of the structure. The resulting local stiffness degradation can, however, be partially compensated through appropriate fibre steering [4,5]. From an engineering perspective, this capability reduces the need for additional local reinforcements while preserving lightweight structural designs and expanding the design space available to engineers compared with conventional constant-stiffness laminates. Consequently, accurate, versatile and effective vibration analysis tools are essential to support the design of advanced variable-stiffness composite cylindrical panels with complex cutout geometries.

The increased design freedom of variable-stiffness laminates, however, also introduces significant modelling challenges. In panels with cutouts, the simultaneous presence of curvature, material anisotropy, spatially varying stiffness, and irregular boundaries complicates both the construction of the structural model and the numerical evaluation of the governing operators. Finite element methods are commonly

E-mail address: alberto.milazzo@unipa.it.

https://doi.org/10.1016/j.tws.2026.115553
Received 10 June 2026; Received in revised form 7 August 2026; Accepted 18 August 2026
Available online 1 September 2026

used for such problems, but they may require substantial preprocessing effort, particularly when curvilinear fibre paths, multiple material regions, or complex cutout geometries must be represented with sufficient accuracy. For this reason, semi-analytical and mesh-independent approaches have attracted considerable attention. Global approximation methods, many of which rely on Ritz formulations [6], are particularly attractive because of their accuracy, convergence properties, and effectiveness in structural modelling.

Early semi-analytical studies on laminated cylindrical panels and shells clarified the effects of boundary conditions, fibre orientation, and lamination schemes on natural frequencies and mode shapes [7–11]. Subsequent developments incorporated shear deformation effects and more general shell kinematics, improving accuracy for moderately thick composite panels [12–16]. Alternative approximation strategies, including mesh-free kp-Ritz methods [17], Chebyshev-based formulations [18], Jacobi polynomial expansions [19], and R-function-based approaches [20], have further extended the applicability of semi-analytical methods to increasingly general boundary conditions and geometries. Recent developments have extended semi-analytical vibration analysis to coupled and multi-component structures, including shell–plate assemblies and combined shell geometries [21–23]. Ritz formulations have also been applied to advanced material systems, including functionally graded and variable-stiffness structures. For functionally graded shells, several contributions have combined Ritz approximations with classical or shear-deformable shell theories [24–26]. For variable-stiffness shells, recent formulations based on orthogonal polynomials, Bézier surface descriptions, and multi-domain strategies have demonstrated the potential of Ritz-type approaches for free vibration and transient dynamic analyses [27–29].

The treatment of cutouts within Ritz formulations has been investigated more extensively for plate structures. Multi-region and plate-assembly approaches have been proposed to represent rectangular or arbitrarily shaped cutouts (e.g., [30,31]), while alternative single-domain descriptions have been developed using discrete Ritz methods [32], R-functions [33,34], energy subtraction techniques [35,36], and implicit geometric representations coupled with high-order quadrature [37]. Some of these methods have been extended to variable-stiffness plates, confirming their effectiveness for complex anisotropic configurations [33,37,38]. Related studies have also proposed trimmed isogeometric formulations for layerwise composite plates with arbitrary cutouts and straight or curvilinear fibres [39], application of the Galerkin and Ritz methods to advanced composite structures such as rotating blades [40] and smart panels [41], while optimization-oriented works have emphasized the role of fibre continuity and manufacturing-related constraints in variable-stiffness laminates with regular and irregular holes [42]. More recently, studies on dynamic modelling, identification, and active vibration control of advanced composite structures have further demonstrated the continuing interest in computational methods for structural dynamics [43–45].

By contrast, the extension of such strategies to curved panel structures remains less developed. The presence of curvature increases the complexity of the kinematic relations, admissible functions, and numerical integration over irregular domains. Available Ritz-based studies for cylindrical panels with cutouts are therefore comparatively limited and have mainly relied on energy-subtraction approaches [46–48] or, more recently, on implicit geometric descriptions combined with high-order quadrature schemes [49].

Despite the significant progress achieved in recent years, existing approaches generally address only a subset of the modelling capabilities required for the vibration analysis of practical composite cylindrical panels. In particular, the combined treatment of arbitrary multiple cutout geometries, variable-stiffness laminates, non-uniform thickness distributions, and multi-region configurations within a unified single-domain framework has not yet been reported. Consequently, the development of a computational framework capable of simultaneously accommodating these features remains an important research challenge.

To address this gap, building on ingredients developed in earlier studies [37,49], the present work proposes a unified computational framework for the free vibration analysis of composite cylindrical panels with variable stiffness and complex cutout geometries. The approach integrates: (i) geometry-independent global approximation functions based on Legendre polynomials and boundary functions; (ii) implicit level-set representations of arbitrary and multiple cutouts; (iii) high-order quadrature for accurate integration over geometrically complex domains; and (iv) a laminate description capable of accommodating curvilinear fibre paths, non-uniform thickness distributions, and multi-region configurations. To the authors' knowledge, a unified single-domain framework that simultaneously accommodates variable-stiffness laminates, complex cutout geometries, non-uniform thickness distributions, and multi-region configurations in cylindrical panels has not been previously reported. The resulting framework retains a geometry-independent discretization while enabling the analysis of cylindrical panels exhibiting complex stiffness distributions and geometric discontinuities. Its accuracy is demonstrated through comparisons with high-fidelity finite element solutions, and representative applications highlight its effectiveness for analysing and tailoring the vibration response of advanced composite structures.

The paper is organized as follows. Section 2 presents the theoretical formulation, including the geometry description, shell kinematics, constitutive modelling and the derivation of the governing equations. Section 3 presents the discretization strategy and the numerical integration procedure for implicitly defined cutout domains. Section 4 presents the validation studies and representative applications of the proposed framework. Finally, Section 5 summarizes the main conclusions and outlines possible future developments.

2. Formulation

Let us consider a circular cylindrical panel having an internal radius R, an opening angle $2\alpha = a/R$, and an axial length $2L$. The panel contains one or more cutouts of arbitrary shape and position. It is constrained along its external edges, whereas the cutout boundaries are free. For modelling purposes, the panel may be partitioned into cylindrical sub-regions bounded by selected circular sections and generators; each sub-region is considered as a variable-stiffness laminate with a general layup. It is worth noting that the concept of *single-domain* adopted in the present work refers to the use of a single global approximation of the displacement field over the entire panel domain. The partitioning of the panel into sub-regions is introduced solely to describe spatial variations in laminate properties, thickness distributions, fibre-path descriptions, or reinforcing regions. Accordingly, the proposed formulation does not rely on independent displacement approximations or interface continuity constraints between adjacent regions, as required in conventional domain-decomposition approaches. A schematic of the geometry is shown in Fig. 1(a).

The proposed formulation is developed within the framework of a geometrically linear first-order shear deformation shell theory and assumes linear elastic constitutive behaviour. Accordingly, material and geometric nonlinearities, manufacturing-induced defects, progressive damage, and rate-dependent material behaviour are beyond the scope of the present model.

2.1. Geometry description

Within the framework of shell structural theories, the geometry of the panel is described by its mid-surface, which, in the absence of cutouts, occupies the domain Ω. The domain Ω is defined in a Cartesian coordinate system whose origin is located at the centre of the panel planform. The x_1 and x_2 axes lie on the panel planform and are aligned with the projections of the cylinder circular sections and generators, respectively, while the x_3 axis is oriented normal to the planform (see

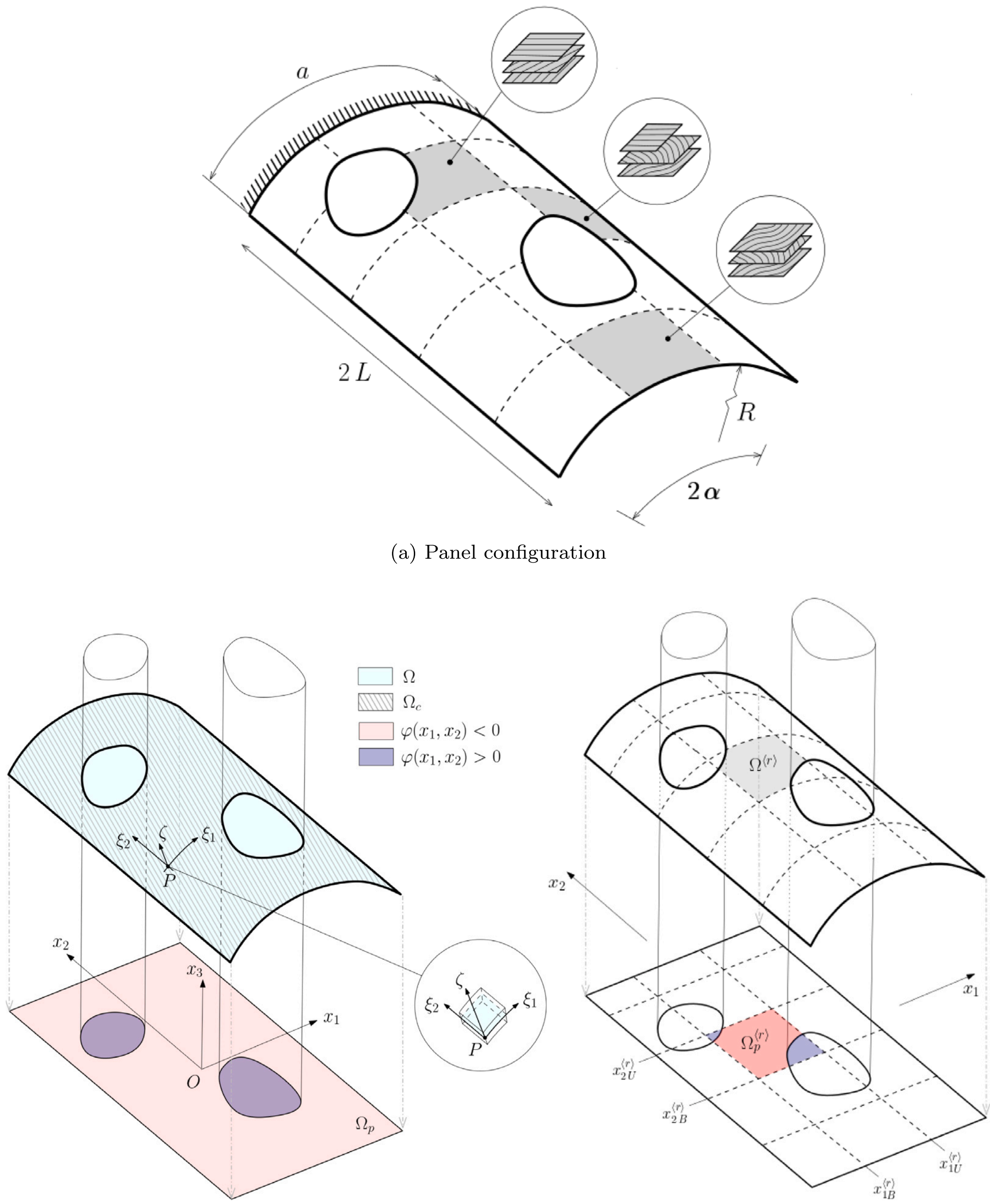

(a) Panel configuration

(b) Mid-surface domains and cutouts definition.

(c) Panel sub-region definition.

Fig. 1. Cylindrical panel geometrical description.

Fig. 1(b)). The planform domain is denoted by $\Omega_p \equiv [-R\sin\alpha, R\sin\alpha] \times [-L, L] \times \{0\}$.

Any through-the-thickness cutouts are generated by intersecting the pristine panel mid-surface Ω with cylinders of suitable cross-section whose axis is aligned with the x_3 direction, as illustrated in Fig. 1(b). The cutout geometry is implicitly described by means of a *level set* function φ [50], which is expressed in terms of the Cartesian coordinates x_1 and x_2, such that $\varphi = \varphi(x_1, x_2)$. Accordingly, the mid-surface domain of the cut panel, denoted by Ω_c, is identified as the subset of Ω where the level set function assumes negative values (see Fig. 1(b)):

$$\Omega_c \equiv \{(x_1, x_2, x_3) \in \Omega \ : \ \varphi(x_1, x_2) < 0\}. \tag{1}$$

Analogously, referring to Fig. 1(c), let us denote by ${\Omega_c}^{\langle r\rangle}$ $(r = 1, \dots, N_r)$ the mid-surface part representative of the rth sub-region of the panel. It corresponds to the planform subdomain ${\Omega_p}^{\langle r\rangle} \equiv \left[x^{\langle r\rangle}_{1\,B}, x^{\langle r\rangle}_{1\,U}\right] \times \left[x^{\langle r\rangle}_{2\,B}, x^{\langle r\rangle}_{2\,U}\right] \times \{0\}$ where $x^{\langle r\rangle}_{i\,B}$ and $x^{\langle r\rangle}_{i\,U}$ are the lower and upper bounds of the x_i coordinate defining the considered sub-region. For ${\Omega_c}^{\langle r\rangle}$ the following implicit representation holds

$${\Omega_c}^{\langle r\rangle} \equiv \{(x_1, x_2, x_3) \in \Omega \ : \ x^{\langle r\rangle}_{1\,B} < x_1 < x^{\langle r\rangle}_{1\,U},\ x^{\langle r\rangle}_{2\,B} < x_2 < x^{\langle r\rangle}_{2\,U},\ \varphi(x_1, x_2) < 0\}. \tag{2}$$

It is worth emphasizing that, in the absence of cutouts, the domain Ω_c coincides with Ω and if the panel has a single sub-region $\Omega_c^{\langle 1\rangle}$ it coincides with Ω_c.

To describe the mechanical behaviour of the panel, a curvilinear orthogonal coordinate system (ξ_1, ξ_2, ζ) is introduced. The coordinates ξ_1 and ξ_2 parameterize the panel mid-surface Ω along the circumferential direction and the cylinder generators, respectively, whereas ζ denotes the thickness coordinate measured along the normal to the mid-surface. Finally, introducing the natural coordinates ξ and η spanning the reference domain $Q \equiv [-1, 1] \times [-1, 1]$, which parameterize the panel mid-surface Ω, the coordinates of a point on the uncut panel mid-surface Ω are expressed as

$$\begin{Bmatrix} x_1 \\ x_2 \\ x_3 \end{Bmatrix} = \begin{Bmatrix} R\sin\left(\frac{\xi_1}{R}\right) \\ \xi_2 \\ R\left[\cos\left(\frac{\xi_1}{R}\right) - \cos\alpha\right] \end{Bmatrix} = \begin{Bmatrix} R\sin(\alpha\xi) \\ L\eta \\ R\left[\cos(\alpha\xi) - \cos\alpha\right] \end{Bmatrix}. \tag{3}$$

It is worth noting that Eq. (3) allows the level-set function φ to be expressed in terms of the curvilinear coordinates ξ_1 and ξ_2 or the natural coordinates ξ and η. Examples of cutout shapes and the associated *level set* functions are given in Appendix A.

2.2. Panel kinematics

For thin to moderately thick panels, the first-order shear deformation theory (FSDT) provides an accurate and computationally efficient framework for a broad class of engineering applications [51–54], including the class of problems addressed in the present work. For very thick laminates or higher-frequency vibration modes, however, higher-order shell theories may provide improved accuracy at the expense of increased computational complexity. The displacement field at a generic point $P \equiv (x_1, x_2, x_3) \equiv (\xi_1, \xi_2, \zeta)$ is expressed as

$$\boldsymbol{d} = \boldsymbol{u} + \left(\zeta + \zeta_0\right) \boldsymbol{L}\boldsymbol{\vartheta}, \tag{4}$$

where $\boldsymbol{d} = \left\{d_{\xi_1} \quad d_{\xi_2} \quad d_{\zeta}\right\}^T$ collects the displacement components along the ξ_1, ξ_2, and ζ directions whereas ζ_0 sets an offset for the thickness position of the modelling reference surface [52]. In Eq. (4), the generalized displacement vectors are defined as $\boldsymbol{u} = \left\{u_{\xi_1} \quad u_{\xi_2} \quad u_{\zeta}\right\}^T$ and $\boldsymbol{\vartheta} = \left\{\vartheta_{\xi_1} \quad \vartheta_{\xi_2}\right\}^T$, where u_{ξ_1}, u_{ξ_2}, and u_ζ are the mid-surface translations along ξ_1, ξ_2, and ζ, respectively, while ϑ_{ξ_1} and ϑ_{ξ_2} are the rotations of a transverse normal about the ξ_2 and ξ_1 axes, respectively [52]. The matrix $\boldsymbol{L}$ is defined as

$$\boldsymbol{L} = \begin{bmatrix} 1 & 0 & 0 \\ 0 & 1 & 0 \end{bmatrix}^T. \tag{5}$$

The strain components e_{ij} follow from the linear strain–displacement relations [52]. They are conveniently arranged into the in-plane and transverse shear strain vectors as

$$\boldsymbol{e}_p = \begin{Bmatrix} e_{11} \\ e_{22} \\ e_{12} \end{Bmatrix} = \boldsymbol{Z}\boldsymbol{\varepsilon} + \left(\zeta + \zeta_0\right) \boldsymbol{Z}\boldsymbol{\kappa}, \tag{6a}$$

$$\boldsymbol{e}_n = \begin{Bmatrix} e_{31} \\ e_{32} \end{Bmatrix} = \widetilde{\mathfrak{Z}}\boldsymbol{\gamma}, \tag{6b}$$

where the generalized strain vectors are defined as

$$\boldsymbol{\varepsilon} = \mathfrak{D}_{pu}\boldsymbol{u}, \tag{7a}$$

$$\boldsymbol{\kappa} = \mathfrak{D}_{p\vartheta}\boldsymbol{\vartheta}, \tag{7b}$$

$$\boldsymbol{\gamma} = \boldsymbol{\vartheta} + \mathfrak{D}_{nu}\boldsymbol{u}, \tag{7c}$$

and the thickness-dependent operators read

$$\mathfrak{Z} = \begin{bmatrix} \frac{1}{(1+\zeta/R)} & 0 & 0 & 0 \\ 0 & 1 & 0 & 0 \\ 0 & 0 & \frac{1}{(1+\zeta/R)} & 1 \end{bmatrix}, \tag{8a}$$

$$\widetilde{\mathfrak{Z}} = \begin{bmatrix} \frac{1}{(1+\zeta/R)} & 0 \\ 0 & 1 \end{bmatrix}. \tag{8b}$$

Finally, the differential operators appearing in Eq. (7) are defined as

$$\mathfrak{D}_{pu} = \begin{bmatrix} \frac{\partial}{\partial \xi_1} & 0 & \frac{1}{R} \\ 0 & \frac{\partial}{\partial \xi_2} & 0 \\ 0 & \frac{\partial}{\partial \xi_1} & 0 \\ \frac{\partial}{\partial \xi_2} & 0 & 0 \end{bmatrix}, \tag{9a}$$

$$\mathfrak{D}_{p\vartheta} = \begin{bmatrix} \frac{\partial}{\partial \xi_1} & 0 \\ 0 & \frac{\partial}{\partial \xi_2} \\ 0 & \frac{\partial}{\partial \xi_1} \\ \frac{\partial}{\partial \xi_2} & 0 \end{bmatrix}, \tag{9b}$$

$$\mathfrak{D}_{nu} = \begin{bmatrix} -\frac{1}{R} & 0 & \frac{\partial}{\partial \xi_1} \\ 0 & 0 & \frac{\partial}{\partial \xi_2} \end{bmatrix}. \tag{9c}$$

2.3. Generalized stress

The stress measures that are energetically conjugate to the generalized strain components in the FSDT shell theory, namely the generalized stresses, are the membrane force resultants per unit length $\boldsymbol{N}$, the bending and twisting moment resultants per unit length $\boldsymbol{M}$, and the transverse shear force resultants per unit length $\boldsymbol{T}$. The generalized stresses are obtained by integrating the stress vectors $\boldsymbol{\sigma}_p = \{\sigma_{11} \quad \sigma_{22} \quad \sigma_{12}\}^T$ and $\boldsymbol{\sigma}_n = \{\sigma_{31} \quad \sigma_{32}\}^T$ through the thickness coordinate.

At the generic point identified by the curvilinear coordinates ξ_1 and ξ_2 the generalized stress resultants corresponding to the generalized strain measures of Eq. (7) assume the following form [52,55]:

$$\boldsymbol{N}\left(\xi_1,\, \xi_2\right) = \int_h \mathfrak{Z}^T \boldsymbol{\sigma}_p \left(1 + \frac{\zeta}{R}\right) \mathrm{d}\zeta, \tag{10a}$$

$$\boldsymbol{M}\left(\xi_1,\, \xi_2\right) = \int_h \mathfrak{Z}^T \boldsymbol{\sigma}_p \left(\zeta + \zeta_0\right) \left(1 + \frac{\zeta}{R}\right) \mathrm{d}\zeta, \tag{10b}$$

$$\boldsymbol{T}\left(\xi_1,\, \xi_2\right) = \boldsymbol{K}_S \int_h \widetilde{\mathfrak{Z}}^T \boldsymbol{\sigma}_n \left(1 + \frac{\zeta}{R}\right) \mathrm{d}\zeta, \tag{10c}$$

where h denotes the local panel thickness, which may vary spatially over the panel. In Eq. (10c), $\mathbf{K}_S = \mathbf{K}_S(\xi_1, \xi_2)$ is a 2×2 local transverse-shear correction operator [51,52]. It modifies the shear stiffness obtained by direct through-thickness integration of the FSDT constitutive relations, so as to enforce energy equivalence with a reconstructed through-thickness shear-stress field. In the proposed approach, the correction operator is evaluated from the local laminate configuration through the Whitney–Pagano energy-equivalence procedure [56, 57], following the formulation reported for laminated composite shell sections in the Abaqus documentation [58].

2.4. Stiffness and inertia properties

Any region $\Omega_c^{\langle r \rangle}$ of the panel is assumed to behave as a laminate composed of $N_L^{\langle r \rangle}$ variable-stiffness layers. Spatial variability may arise from variations in the ply thickness, material heterogeneity within the layer, or the presence of curvilinear fibre paths in fibre-reinforced plies. Constant-stiffness laminates, either isotropic or anisotropic, are recovered as special cases of this general formulation. The layup of each region is therefore described by associating with each ply of the stacking sequence a set of spatially dependent fields defining the local material properties, thickness distribution, and material orientation. Denoting by the superscript $\bullet^{(r,k)}$ quantities associated with the kth ply of the rth region layup, the ply behaviour is characterized by the following fields:

- $\boldsymbol{E}^{(r,k)}(\xi_1, \xi_2)$, the vector of ply material properties expressed in the orthotropic material reference system, namely the Young's moduli

$E_1^{(r,k)}$ and $E_2^{(r,k)}$, the Poisson's ratio $\nu_{12}^{(r,k)}$, the shear moduli $G_{12}^{(r,k)}$, $G_{13}^{(r,k)}$ and $G_{23}^{(r,k)}$, and the material density $\rho^{(r,k)}$;
- $t^{(r,k)}(\xi_1, \xi_2)$, defining the thickness distribution of the ply;
- $\theta^{(r,k)}(\xi_1, \xi_2)$, the material orientation angle measured between the principal orthotropic axis and the ξ_1 direction. For fibre-reinforced layers, this quantity coincides with the local fibre orientation associated with the deposition path.

Accordingly, the stacking sequence of the rth subregion is described by the list of spatial fields $\left[\ldots/\left\{\boldsymbol{E}^{(r,k)}(\xi_1,\xi_2),\, t^{(r,k)}(\xi_1,\xi_2),\, \theta^{(r,k)}(\xi_1,\xi_2)\right\}/\ldots\right]$ which define the laminate architecture. The constitutive equations of each ply are determined by accounting for the local material composition and orientation. Under the plane stress assumption ($\sigma_{33} = 0$), they take the form [52]

$$\begin{Bmatrix} \boldsymbol{\sigma}_p{}^{(r,k)} \\ \boldsymbol{\sigma}_n{}^{(r,k)} \end{Bmatrix} = \begin{bmatrix} \boldsymbol{Q}_p{}^{(r,k)} & \boldsymbol{0} \\ \boldsymbol{0} & \boldsymbol{Q}_n{}^{(r,k)} \end{bmatrix} \begin{Bmatrix} \boldsymbol{e}_p \\ \boldsymbol{e}_n \end{Bmatrix}. \tag{11}$$

The coefficients of the ply stiffness matrices $\boldsymbol{Q}_p{}^{(r,k)}$ and $\boldsymbol{Q}_n{}^{(r,k)}$ are given by

$$Q_{p11}{}^{(r,k)}(\xi_1,\, \xi_2) = \bar{Q}_{11}{}^{(r,k)}c^4 + 2\left[\bar{Q}_{12}{}^{(r,k)} + 2\bar{Q}_{33}{}^{(r,k)}\right]s^2c^2 + \bar{Q}_{22}{}^{(r,k)}s^4 \tag{12a}$$

$$Q_{p12^{(r,k)}}(\xi_1,\, \xi_2) = \bar{Q}_{12}{}^{(r,k)}c^4 + \left[\bar{Q}_{11}{}^{(r,k)} + \bar{Q}_{22}{}^{(r,k)} - 4\bar{Q}_{33}{}^{(r,k)}\right]s^2c^2 + \bar{Q}_{12}{}^{(r,k)}s^4, \tag{12b}$$

$$Q_{p22}{}^{(r,k)}(\xi_1,\, \xi_2) = \bar{Q}_{11}{}^{(r,k)}s^4 + 2\left[\bar{Q}_{12}{}^{(r,k)} + 2\bar{Q}_{33}{}^{(r,k)}\right]s^2c^2 + \bar{Q}_{22}{}^{(r,k)}c^4, \tag{12c}$$

$$\begin{aligned} Q_{p13}{}^{(r,k)}(\xi_1,\, \xi_2) &= \left[\bar{Q}_{11}{}^{(r,k)} - \bar{Q}_{12}{}^{(r,k)} - 2\bar{Q}_{33}{}^{(r,k)}\right]sc^3 \\ &+ \left[\bar{Q}_{12}{}^{(r,k)} - \bar{Q}_{22}{}^{(r,k)} + 2\bar{Q}_{33}{}^{(r,k)}\right]s^3c, \end{aligned} \tag{12d}$$

$$\begin{aligned} Q_{p23}{}^{(r,k)}(\xi_1,\, \xi_2) &= \left[\bar{Q}_{11}{}^{(r,k)} - \bar{Q}_{12}{}^{(r,k)} - 2\bar{Q}_{33}{}^{(r,k)}\right]s^3c \\ &+ \left[\bar{Q}_{12}{}^{(r,k)} - \bar{Q}_{22}{}^{(r,k)} + 2\bar{Q}_{33}{}^{(r,k)}\right]sc^3, \end{aligned} \tag{12e}$$

$$\begin{aligned} Q_{p33}{}^{(r,k)}(\xi_1,\, \xi_2) &= \left[\bar{Q}_{11}{}^{(r,k)} + \bar{Q}_{22}{}^{(r,k)} - 2\bar{Q}_{12}{}^{(r,k)} - 2\bar{Q}_{33}{}^{(r,k)}\right]s^2c^2 \\ &+ \bar{Q}_{33}{}^{(r,k)}\left[s^4 + c^4\right], \end{aligned} \tag{12f}$$

$$Q_{n11}{}^{(r,k)}(\xi_1,\, \xi_2) = \bar{Q}_{44}{}^{(r,k)}c^2 + \bar{Q}_{55}{}^{(r,k)}s^2, \tag{12g}$$

$$Q_{n12}{}^{(r,k)}(\xi_1,\, \xi_2) = \left[\bar{Q}_{55}{}^{(r,k)} - \bar{Q}_{44}{}^{(r,k)}\right]cs, \tag{12h}$$

$$Q_{n22}{}^{(r,k)}(\xi_1,\, \xi_2) = \bar{Q}_{44}{}^{(r,k)}s^2 + \bar{Q}_{55}{}^{(r,k)}c^2, \tag{12i}$$

where $c = \cos\theta(\xi_1,\, \xi_2)$, $s = \sin\theta(\xi_1,\, \xi_2)$ and

$$\bar{Q}_{11}{}^{(r,k)}(\xi_1,\, \xi_2) = \frac{E_1^{(r,k)}(\xi_1,\, \xi_2)}{1 - \nu_{12}^{(r,k)}(\xi_1,\, \xi_2)\,\nu_{21}^{(r,k)}(\xi_1,\, \xi_2)}, \tag{13a}$$

$$\bar{Q}_{22}{}^{(r,k)}(\xi_1,\, \xi_2) = \frac{E_2{}^{(r,k)}(\xi_1,\, \xi_2)}{1 - \nu_{12}^{(r,k)}(\xi_1,\, \xi_2)\,\nu_{21}^{(r,k)}(\xi_1,\, \xi_2)}, \tag{13b}$$

$$\bar{Q}_{12}{}^{(r,k)}(\xi_1,\, \xi_2) = \frac{\nu_{12}^{(r,k)}(\xi_1,\, \xi_2)\,E_2^{(r,k)}(\xi_1,\, \xi_2)}{1 - \nu_{12}^{(r,k)}(\xi_1,\, \xi_2)\,\nu_{21}^{(r,k)}(\xi_1,\, \xi_2)}, \tag{13c}$$

$$\bar{Q}_{33}{}^{(r,k)}(\xi_1,\, \xi_2) = G_{12}{}^{(r,k)}(\xi_1,\, \xi_2), \tag{13d}$$

$$\bar{Q}_{44}{}^{(r,k)}(\xi_1,\, \xi_2) = G_{13}{}^{(r,k)}(\xi_1,\, \xi_2), \tag{13e}$$

$$\bar{Q}_{55}{}^{(r,k)}(\xi_1,\, \xi_2) = G_{23}{}^{(r,k)}(\xi_1,\, \xi_2), \tag{13f}$$

being $\nu_{21}^{(r,k)}(\xi_1,\, \xi_2) = E_2^{(r,k)}(\xi_1,\, \xi_2)\,\nu_{12}^{(r,k)}(\xi_1,\, \xi_2)/E_1^{(r,k)}(\xi_1,\, \xi_2)$ the reciprocal Poisson's ratio. Substituting the ply constitutive relations, Eq. (11), into the generalized stress definitions, Eq. (10), yields the laminate constitutive law for the rth panel subregion

$$\begin{Bmatrix} \boldsymbol{N} \\ \boldsymbol{M} \\ \boldsymbol{T} \end{Bmatrix} = \begin{bmatrix} \boldsymbol{A}^{\langle r \rangle} & \boldsymbol{B}^{\langle r \rangle} & \boldsymbol{0} \\ \boldsymbol{B}^{\langle r \rangle} & \boldsymbol{D}^{\langle r \rangle} & \boldsymbol{0} \\ \boldsymbol{0} & \boldsymbol{0} & \boldsymbol{A}_S{}^{\langle r \rangle} \end{bmatrix} \begin{Bmatrix} \boldsymbol{\varepsilon} \\ \boldsymbol{\kappa} \\ \boldsymbol{\gamma} \end{Bmatrix}, \tag{14}$$

where $\boldsymbol{A}^{\langle r \rangle} = \boldsymbol{A}_0{}^{\langle r \rangle}$, $\boldsymbol{B}^{\langle r \rangle} = \boldsymbol{A}_1{}^{\langle r \rangle}$, $\boldsymbol{D}^{\langle r \rangle} = \boldsymbol{A}_2{}^{\langle r \rangle}$ and $\boldsymbol{A}_S{}^{\langle r \rangle}$ denote the laminate membrane, coupling, bending and transverse shear stiffness matrices, respectively, defined as

$$\boldsymbol{A}_m{}^{\langle r \rangle}(\xi_1, \xi_2) = \sum_{k=1}^{N_L^r} \int_{h_{k-1}}^{h_k} \boldsymbol{Z}^T \boldsymbol{Q}_p{}^{(r,k)} \boldsymbol{Z}\,(\zeta + \zeta_0)^m \left(1 + \frac{\zeta}{R}\right) \mathrm{d}\zeta, \qquad m = 0, 1, 2, \tag{15a}$$

$$\begin{aligned} \boldsymbol{A}_S{}^{\langle r \rangle}(\xi_1,\, \xi_2) &= \boldsymbol{K}_S(\xi_1, \xi_2) \sum_{k=1}^{N_L{}^{\langle r \rangle}} \int_{h_{k-1}}^{h_k} \widetilde{\boldsymbol{\mathfrak{Z}}}^T \boldsymbol{Q}_n{}^{(r,k)} \widetilde{\boldsymbol{\mathfrak{Z}}}\ (1 + \zeta/R)\,\mathrm{d}\zeta \\ &= \boldsymbol{K}_S(\xi_1, \xi_2)\boldsymbol{A}_{S,0}^{\langle r \rangle}(\xi_1, \xi_2). \end{aligned} \tag{15b}$$

Here h_{k-1} and h_k are the ζ-coordinates of the bottom and top surfaces of the kth ply. Since the ply thickness is described by the spatial field $t^{(r,k)} = t^{(r,k)}(\xi_1,\, \xi_2)$, h_{k-1} and h_k are also functions of (ξ_1, ξ_2). In Eq. (15b), $\mathbf{A}_{S,0}^{\langle r \rangle}$ denotes the transverse-shear stiffness obtained by direct through-thickness integration of the FSDT constitutive relations, whereas $\mathbf{A}_S^{\langle r \rangle}$ is the corresponding energy-equivalent corrected stiffness and, accordingly, $\boldsymbol{K}_S = \boldsymbol{A}_S^{\langle r \rangle}\left(\boldsymbol{A}_{S,0}^{\langle r \rangle}\right)^{-1}$.

Finally, introducing the thickness moments of the density field

$$I_m{}^{\langle r \rangle}(\xi_1,\, \xi_2) = \sum_{k=1}^{N_L^r} \int_{h_{k-1}}^{h_k} \rho^{(r,k)}(\xi_1, \xi_2)\ \left[\zeta + \zeta_0\right]^m \left[1 + \frac{\zeta}{R}\right] \mathrm{d}\zeta, \qquad m = 0, 1, 2, \tag{16}$$

the inertia matrices of the rth panel subregion can be written as

$$\boldsymbol{I}_{uu}{}^{\langle r \rangle} = I_0{}^{\langle r \rangle}\,\boldsymbol{I}_{3\times 3}, \tag{17a}$$

$$\boldsymbol{I}_{u\vartheta}{}^{\langle r \rangle} = \boldsymbol{I}_{\vartheta u}{}^{\langle r \rangle T} = I_1{}^{\langle r \rangle}\,\boldsymbol{L}, \tag{17b}$$

$$\boldsymbol{I}_{\vartheta\vartheta}{}^{\langle r \rangle} = I_2{}^{\langle r \rangle}\,\boldsymbol{L}^T\boldsymbol{L}, \tag{17c}$$

where $\boldsymbol{I}_{3\times 3}$ is the 3×3 identity matrix.

2.5. Governing equations

Assuming that the kinematical boundary conditions are satisfied, the governing equations of the panel follow from the stationarity condition of the energy functional with respect to the primary variables of the problem, namely the generalized displacements [59]. For the free vibration problem, the energy functional consists of the strain and kinetic energy contributions and can be written as

$$\begin{aligned} \Pi &= \frac{1}{2}\int_{\Omega_c} \left(\boldsymbol{\varepsilon}^T\boldsymbol{N} + \boldsymbol{\kappa}^T\boldsymbol{M} + \boldsymbol{\gamma}^T\boldsymbol{T}\right)\mathrm{d}\Omega \\ &- \omega^2 \int_{\Omega_c} \frac{1}{2}\left(\boldsymbol{u}^T\boldsymbol{I}_{uu}\boldsymbol{u} + \boldsymbol{u}^T\boldsymbol{I}_{u\vartheta}\boldsymbol{\vartheta} + \boldsymbol{\vartheta}^T\boldsymbol{I}_{\vartheta u}\boldsymbol{u} + \boldsymbol{\vartheta}^T\boldsymbol{I}_{\vartheta\vartheta}\boldsymbol{\vartheta}\right)\mathrm{d}\Omega, \end{aligned} \tag{18}$$

where ω denotes the circular frequency. Recalling that $\Omega_c \equiv \cup_{r=1}^{N_r}\Omega_c{}^{\langle r \rangle}$, and introducing the laminate constitutive relations given in Eq. (14), the functional Π can be rewritten as

$$\begin{aligned} \Pi = &\sum_{r=1}^{N_r}\frac{1}{2}\int_{\Omega_c{}^{\langle r \rangle}} \left(\boldsymbol{\varepsilon}^T\boldsymbol{A}^{\langle r \rangle}\boldsymbol{\varepsilon} + \boldsymbol{\varepsilon}^T\boldsymbol{B}^{\langle r \rangle}\boldsymbol{\kappa} + \boldsymbol{\kappa}^T\boldsymbol{B}^{\langle r \rangle}\boldsymbol{\varepsilon} + \boldsymbol{\kappa}^T\boldsymbol{D}^{\langle r \rangle}\boldsymbol{\kappa} + \boldsymbol{\gamma}^T\boldsymbol{A}_S{}^{\langle r \rangle}\boldsymbol{\gamma}\right)\mathrm{d}\Omega \\ &- \omega^2\sum_{r=1}^{N_r}\int_{\Omega_c{}^{\langle r \rangle}} \frac{1}{2}\left(\boldsymbol{u}^T\boldsymbol{I}_{uu}{}^{\langle r \rangle}\boldsymbol{u} + \boldsymbol{u}^T\boldsymbol{I}_{u\vartheta}{}^{\langle r \rangle}\boldsymbol{\vartheta} + \boldsymbol{\vartheta}^T\boldsymbol{I}_{\vartheta u}{}^{\langle r \rangle}\boldsymbol{u} + \boldsymbol{\vartheta}^T\boldsymbol{I}_{\vartheta\vartheta}{}^{\langle r \rangle}\boldsymbol{\vartheta}\right)\mathrm{d}\Omega. \end{aligned} \tag{19}$$

Upon substitution of Eq. (7), the functional becomes explicitly dependent on the generalized displacements and enforcing its stationarity yields the governing equilibrium equations of the panel.

3. Discretization procedure

The governing equations are discretized using global approximation functions defined over the entire panel domain. A variational procedure is employed to determine the discrete equations. From this perspective, the approach is classified within the class of mesh-free methods, which typically reduce model preparation costs by eliminating the need for mesh generation and associated data preprocessing.

Table 1
Correspondence between parametric domain edges and exponents in the boundary function.

Edge	Edge function	Exponent
$\xi = -1$	$(1+\xi)$	a_1
$\xi = 1$	$(1-\xi)$	a_2
$\eta = -1$	$(1+\eta)$	a_3
$\eta = 1$	$(1-\eta)$	a_4

3.1. Trial functions

Different families of trial functions have been employed in the literature [60] and Legendre orthogonal polynomials have proved particularly effective as expansion bases [33,34,37,59]. Thus, the employed trial functions are constructed as the tensor product of one-dimensional Legendre polynomials defined over the natural coordinates ξ and η [37,61]; according to the pb-2 Ritz scheme [62,63], they are modified by embedding a boundary function so that the essential boundary conditions are automatically satisfied.

Let us denote by $\boldsymbol{\phi}_m(\varsigma) = \left\{\phi_0(\varsigma) \quad \phi_1(\varsigma) \quad \dots \quad \phi_{m-1}(\varsigma)\right\}$ the row vector collecting the Legendre polynomials ϕ_i from order $i = 0$ up to $i = m-1$, defined over the interval $\varsigma = [-1, 1]$. For the generalized displacement component $\chi \in \left\{u_{\xi_1}, u_{\xi_2}, u_\zeta, \vartheta_{\xi_1}, \vartheta_{\xi_2}\right\}$ the Ritz approximation is written as

$$\chi = \boldsymbol{\Psi}_\chi \boldsymbol{C}_\chi = f_\chi(\xi, \eta)\hat{\boldsymbol{\Psi}}_\chi \boldsymbol{C}_\chi, \tag{20}$$

where

- $\hat{\boldsymbol{\Psi}}_\chi$ is the $M_\chi N_\chi$ row vector defined as $\hat{\boldsymbol{\Psi}}_\chi = \boldsymbol{\phi}_{M_\chi}(\xi) \otimes \boldsymbol{\phi}_{N_\chi}(\eta)$ with the symbol $\otimes$ denoting the Kronecker matrix product;
- $\boldsymbol{C}_\chi$ is the $M_\chi N_\chi$ column vector containing the Ritz expansion unknown coefficients;
- f_χ is a boundary function, introduced to enforce the essential (kinematic) boundary conditions along the external edges, thereby ensuring kinematic admissibility of the trial functions. Accordingly, $\boldsymbol{\Psi}_\chi = f_\chi(\xi,\eta)\hat{\boldsymbol{\Psi}}_\chi$ denotes the kinematically admissible basis used in Eq. (20).

The boundary function f_χ is defined as

$$f_\chi(\xi,\eta) = (1+\xi)^{a_1}(1-\xi)^{a_2}(1+\eta)^{a_3}(1-\eta)^{a_4}, \tag{21}$$

where each factor corresponds to one edge of the parametric domain, as summarized in Table 1. The exponents $a_i \in \{0,1\}$ are independently assigned according to the essential boundary conditions prescribed for the corresponding generalized displacement along each edge. Specifically, $a_i = 1$ enforces the satisfaction of homogeneous essential boundary conditions (i.e., vanishing displacement), whereas $a_i = 0$ leaves the field variable unconstrained on that boundary segment.

According to the expansion formula of Eq. (20), a compact matrix form can be introduced for the generalized displacement approximations which are given by

$$\boldsymbol{u} = \begin{bmatrix} \boldsymbol{\Psi}_{u_{\xi_1}} & \boldsymbol{0} & \boldsymbol{0} \\ \boldsymbol{0} & \boldsymbol{\Psi}_{u_{\xi_2}} & \boldsymbol{0} \\ \boldsymbol{0} & \boldsymbol{0} & \boldsymbol{\Psi}_{u_\zeta} \end{bmatrix} \begin{Bmatrix} \boldsymbol{C}_{u_{\xi_1}} \\ \boldsymbol{C}_{u_{\xi_2}} \\ \boldsymbol{C}_{u_\zeta} \end{Bmatrix} = \boldsymbol{\Phi}_u \, \boldsymbol{U}, \tag{22a}$$

$$\boldsymbol{\vartheta} = \begin{bmatrix} \boldsymbol{\Psi}_{\vartheta_{\xi_1}} & \boldsymbol{0} \\ \boldsymbol{0} & \boldsymbol{\Psi}_{\vartheta_{\xi_2}} \end{bmatrix} \begin{Bmatrix} \boldsymbol{C}_{\vartheta_{\xi_1}} \\ \boldsymbol{C}_{\vartheta_{\xi_2}} \end{Bmatrix} = \boldsymbol{\Phi}_\vartheta \, \boldsymbol{\Theta}. \tag{22b}$$

Upon substituting Eqs. (22) into Eq. (7), the discretized form of the generalized strain follows as

$$\boldsymbol{\varepsilon} = \boldsymbol{\mathcal{D}}_{pu}\boldsymbol{\Phi}_u\boldsymbol{U} = \begin{bmatrix} \boldsymbol{\Psi}_{u_{\xi_1},\xi_1} & \boldsymbol{0} & \frac{1}{R}\boldsymbol{\Psi}_{u_\zeta} \\ \boldsymbol{0} & \boldsymbol{\Psi}_{u_{\xi_2},\xi_2} & \boldsymbol{0} \\ \boldsymbol{0} & \boldsymbol{\Psi}_{u_{\xi_2},\xi_1} & \boldsymbol{0} \\ \boldsymbol{\Psi}_{u_{\xi_1},\xi_2} & \boldsymbol{0} & \boldsymbol{0} \end{bmatrix} \begin{Bmatrix} \boldsymbol{C}_{u_{\xi_1}} \\ \boldsymbol{C}_{u_{\xi_2}} \\ \boldsymbol{C}_{u_\zeta} \end{Bmatrix} = \boldsymbol{\mathcal{B}}_{pu}\boldsymbol{U}, \tag{23a}$$

$$\boldsymbol{\kappa} = \boldsymbol{\mathcal{D}}_{p\vartheta}\boldsymbol{\Phi}_\vartheta\boldsymbol{\Theta} = \begin{bmatrix} \boldsymbol{\Psi}_{\vartheta_{\xi_1},\xi_1} & \boldsymbol{0} \\ \boldsymbol{0} & \boldsymbol{\Psi}_{\vartheta_{\xi_2},\xi_2} \\ \boldsymbol{0} & \boldsymbol{\Psi}_{\vartheta_{\xi_2},\xi_1} \\ \boldsymbol{\Psi}_{\vartheta_{\xi_1},\xi_2} & \boldsymbol{0} \end{bmatrix} \begin{Bmatrix} \boldsymbol{C}_{\vartheta_{\xi_1}} \\ \boldsymbol{C}_{\vartheta_{\xi_2}} \end{Bmatrix} = \boldsymbol{\mathcal{B}}_{p\vartheta}\boldsymbol{\Theta}, \tag{23b}$$

$$\begin{aligned} \boldsymbol{\gamma} &= \boldsymbol{\Phi}_\vartheta\boldsymbol{\Theta} + \boldsymbol{\mathcal{D}}_{nu}\boldsymbol{\Phi}_u\boldsymbol{U} \\ &= \begin{bmatrix} \boldsymbol{\Psi}_{\vartheta_{\xi_1}} & \boldsymbol{0} \\ \boldsymbol{0} & \boldsymbol{\Psi}_{\vartheta_{\xi_2}} \end{bmatrix} \begin{Bmatrix} \boldsymbol{C}_{\vartheta_{\xi_1}} \\ \boldsymbol{C}_{\vartheta_{\xi_2}} \end{Bmatrix} \\ &\quad + \begin{bmatrix} -\frac{1}{R}\boldsymbol{\Psi}_{u_{\xi_1}} & \boldsymbol{0} & \boldsymbol{\Psi}_{u_\zeta,\xi_1} \\ \boldsymbol{0} & \boldsymbol{0} & \boldsymbol{\Psi}_{u_\zeta,\xi_2} \end{bmatrix} \begin{Bmatrix} \boldsymbol{C}_{u_{\xi_1}} \\ \boldsymbol{C}_{u_{\xi_2}} \\ \boldsymbol{C}_{u_\zeta} \end{Bmatrix} \\ &= \boldsymbol{\Phi}_\vartheta\boldsymbol{\Theta} + \boldsymbol{\mathcal{B}}_{nu}\boldsymbol{U}. \end{aligned} \tag{23c}$$

3.2. Discrete governing equations

The displacement and strain fields expansions, Eqs. (22) and (23), are substituted into the energy functional Π, yielding a discrete quadratic functional in terms of the expansion coefficients. Introducing the vector of generalized unknowns $\boldsymbol{X} = \left\{\boldsymbol{U}^T \quad \boldsymbol{\Theta}^T\right\}^T$, the functional can be recast in the form

$$\Pi(\boldsymbol{X}) = \frac{1}{2}\boldsymbol{X}^T\boldsymbol{K}\boldsymbol{X} - \frac{1}{2}\omega^2\boldsymbol{X}^T\boldsymbol{M}\boldsymbol{X}, \tag{24}$$

where $\boldsymbol{K}$ and $\boldsymbol{M}$ denote the global stiffness and mass matrices, respectively. These are defined as

$$\boldsymbol{M} = \sum_{r=1}^{N_r}\int_{\Omega_c{}^{\langle r\rangle}} \begin{bmatrix} \boldsymbol{\Phi}_u^T\boldsymbol{I}_{uu}{}^{\langle r\rangle}\boldsymbol{\Phi}_u & \boldsymbol{\Phi}_u^T\boldsymbol{I}_{u\vartheta}{}^{\langle r\rangle}\boldsymbol{\Phi}_\vartheta \\ \boldsymbol{\Phi}_\vartheta^T\boldsymbol{I}_{\vartheta u}{}^{\langle r\rangle}\boldsymbol{\Phi}_u & \boldsymbol{\Phi}_\vartheta^T\boldsymbol{I}_{\vartheta\vartheta}{}^{\langle r\rangle}\boldsymbol{\Phi}_\vartheta \end{bmatrix} \mathrm{d}\Omega, \tag{25a}$$

$$\boldsymbol{K} = \sum_{r=1}^{N_r}\int_{\Omega_c{}^{\langle r\rangle}} \begin{bmatrix} \boldsymbol{\mathcal{B}}_{pu}^T\boldsymbol{A}^{\langle r\rangle}\boldsymbol{\mathcal{B}}_{pu} + \boldsymbol{\mathcal{B}}_{nu}^T\boldsymbol{A}_S{}^{\langle r\rangle}\boldsymbol{\mathcal{B}}_{nu} & \boldsymbol{\mathcal{B}}_{pu}^T\boldsymbol{B}^{\langle r\rangle}\boldsymbol{\mathcal{B}}_{p\vartheta} + \boldsymbol{\mathcal{B}}_{nu}^T\boldsymbol{A}_S{}^{\langle r\rangle}\boldsymbol{\Phi}_\vartheta \\ \boldsymbol{\mathcal{B}}_{p\vartheta}^T\boldsymbol{B}^{\langle r\rangle}\boldsymbol{\mathcal{B}}_{pu} + \boldsymbol{\Phi}_\vartheta^T\boldsymbol{A}_S{}^{\langle r\rangle}\boldsymbol{\mathcal{B}}_{nu} & \boldsymbol{\mathcal{B}}_{p\vartheta}^T\boldsymbol{D}^{\langle r\rangle}\boldsymbol{\mathcal{B}}_{p\vartheta} + \boldsymbol{\Phi}_\vartheta^T\boldsymbol{A}_S{}^{\langle r\rangle}\boldsymbol{\Phi}_\vartheta \end{bmatrix} \mathrm{d}\Omega. \tag{25b}$$

Enforcing stationarity of Π with respect to $\boldsymbol{X}$ leads to the generalized eigenvalue problem

$$\left(\boldsymbol{K} - \omega^2\boldsymbol{M}\right)\boldsymbol{X} = \boldsymbol{0}. \tag{26}$$

The solution of Eq. (26) yields the natural circular frequencies of the panel and the associated Ritz coefficients, from which the corresponding vibration mode shapes are reconstructed via Eq. (22).

3.3. Structural operators computation

As established in Eqs. (25a) and (25b), the evaluation of the mass and stiffness matrices involves the integration of complex functions over geometrically complex domains, which requires accurate and efficient numerical quadrature rules. Here, the high-order quadrature algorithm proposed by Saye [64] for integrating functions over domains implicitly defined by level set functions is employed.

Within the geometrical framework introduced in Section 2.1, the region mid-surface $\Omega_c{}^{\langle r\rangle}$ is mapped onto a subset $\widetilde{\Omega}_c{}^{\langle r\rangle}$ of the region

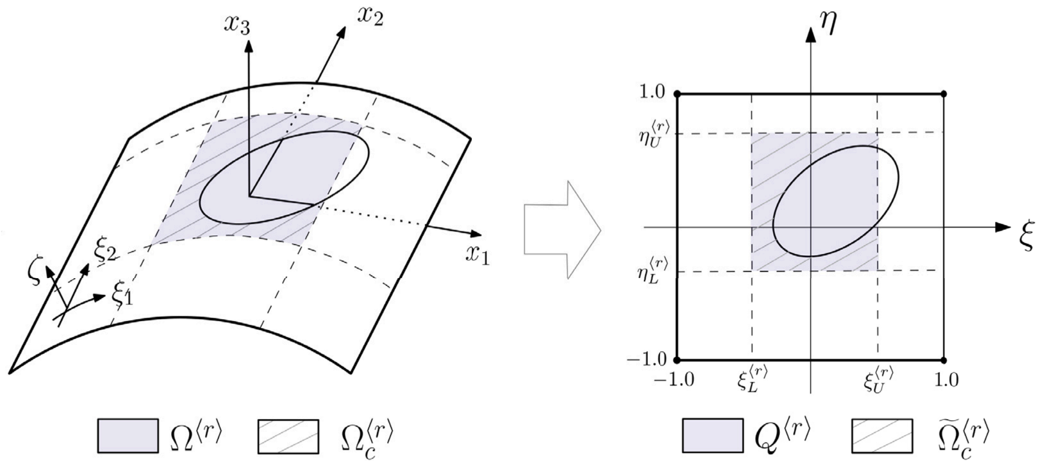

Fig. 2. Region mapping of a cylindrical panel with a *cutout*.

support $Q^{\langle r \rangle} = \left[\xi_L^{\langle r \rangle}, \xi_U^{\langle r \rangle}\right] \times \left[\eta_L^{\langle r \rangle}, \eta_U^{\langle r \rangle}\right]$ in the natural coordinate space (see Fig. 2).

This mapping allows integrals over $\Omega_c{}^{\langle r \rangle}$ to be transferred to $\widetilde{\Omega}_c{}^{\langle r \rangle}$ as

$$\int_{\Omega_c{}^{\langle r \rangle}} f(\xi, \eta)\, \mathrm{d}\Omega = \int_{\widetilde{\Omega}_c{}^{\langle r \rangle}} f(\xi, \eta)\, J(\xi, \eta)\, \mathrm{d}\xi\, \mathrm{d}\eta, \tag{27}$$

where $J(\xi, \eta)$ is the Jacobian determinant associated with the transformation defined by Eqs. (3). The domain $\widetilde{\Omega}_c{}^{\langle r \rangle}$ can be implicitly defined as

$$\widetilde{\Omega}_c{}^{\langle r \rangle} \equiv \left\{ (\xi, \eta) \in Q^{\langle r \rangle} \,:\, \widetilde{\varphi}(\xi, \eta) < 0 \right\}, \tag{28}$$

where the auxiliary level-set function $\widetilde{\varphi}$ is introduced by expressing the level-set function $\varphi(x_1, x_2)$ in terms of natural coordinates

$$\widetilde{\varphi}(\xi, \eta) \equiv \varphi(x_1(\xi, \eta), x_2(\xi, \eta)). \tag{29}$$

This representation enables the use of Saye's high-order quadrature schemes for implicitly defined domains, so that the integrals are evaluated as

$$\int_{\widetilde{\Omega}_c{}^{\langle r \rangle}} f(\xi, \eta)\, J(\xi, \eta)\, \mathrm{d}\xi\, \mathrm{d}\eta \approx \sum_{g=1}^{N_g} f(\xi^g, \eta^g)\, J(\xi^g, \eta^g)\, w^g, \tag{30}$$

where (ξ^g, η^g) and w^g are the quadrature points and weights, respectively, and N_g is their total number.

The algorithm that determines the points and weights of the quadrature rule is briefly described in the following for the sake of completeness; for further details, the reader is referred to [64]. The support domain $Q^{\langle r \rangle}$ is recursively partitioned into subdomains Q_k such that, within each subdomain, $\widetilde{\varphi}$ is either strictly negative, strictly positive, or sign-changing while remaining monotone along either the ξ- or η-direction. If none of these conditions is satisfied, the domain is bisected along the coordinate direction corresponding to the smaller magnitude of the gradient of $\widetilde{\varphi}$. The procedure is applied recursively until all subdomains satisfy one of the above criteria. Quadrature rules are constructed independently on each subdomain Q_k. If Q_k lies entirely within $\widetilde{\Omega}_c$, standard tensor-product Gauss quadrature is employed. Conversely, if Q_k lies entirely outside $\widetilde{\Omega}_c$, it does not contribute to the integral. In the case where Q_k is intersected by the zero level set of $\widetilde{\varphi}$, a specialized procedure is adopted. Owing to the enforced sign consistency of the gradient, $\widetilde{\varphi}$ admits at most one zero along either the ξ- or η-direction for fixed values of the other coordinate. Without loss of generality, and with reference to the example scheme shown in Fig. 3, assume that the level set function remains monotone along the ξ-direction and zeros occur along the η-direction. The integral of a function f over $Q_k = [\xi_L, \xi_U] \times [\eta_L, \eta_U]$ can then be expressed as

$$\int_{Q_k} f(\xi, \eta)\, \mathrm{d}\xi\, \mathrm{d}\eta = \sum_{i=1}^{n+1} \int_{I_\eta^i} \left[\int_{I_\xi(\eta)} f(\xi, \eta)\, \mathrm{d}\xi \right] \mathrm{d}\eta, \tag{31}$$

where the intervals $I_\eta^i = [\eta_{i-1}, \eta_i]$ are constructed from the ordered set $\{\eta_0, \ldots, \eta_{n+1}\}$ comprising η_L, η_U, and the zeros of $\widetilde{\varphi}(\xi_L, \eta)$ and $\widetilde{\varphi}(\xi_U, \eta)$. For each fixed $\bar{\eta}$, the integration interval $I_\xi(\bar{\eta})$ depends on the sign of $\widetilde{\varphi}$. Denoting by $\bar{\xi}$ the possible zero of $\widetilde{\varphi}(\xi, \bar{\eta})$, it follows that

$$I_\xi(\bar{\eta}) = \begin{cases} [\ \xi_L,\ \bar{\xi}\ ] & \text{if } \widetilde{\varphi}\left(\frac{\xi_L + \bar{\xi}}{2}, \bar{\eta}\right) < 0, \\ [\bar{\xi}, \xi_U] & \text{if } \widetilde{\varphi}\left(\frac{\xi_L + \bar{\xi}}{2}, \bar{\eta}\right) > 0, \end{cases} \tag{32}$$

whereas if no zero is found

$$I_\xi(\bar{\eta}) = \begin{cases} [\xi_L, \xi_U] & \text{if } \widetilde{\varphi}\left(\frac{\xi_L + \xi_U}{2}, \bar{\eta}\right) < 0, \\ \emptyset & \text{if } \widetilde{\varphi}\left(\frac{\xi^L + \xi^U}{2}, \bar{\eta}\right) > 0. \end{cases} \tag{33}$$

One-dimensional Gauss quadrature is applied over each interval I_η^i and, for every corresponding integration point, over the associated interval $I_\xi(\eta)$, yielding the two-dimensional quadrature points and weights. More specifically, for cut subdomains the two-dimensional quadrature rule is obtained as a nested product of one-dimensional Gauss rules. The resulting weights are computed as the product of the outer and inner one-dimensional Gauss weights, including the corresponding interval-scaling factors, while the geometric Jacobian $J(\xi, \eta)$ is evaluated at each quadrature point and included in the integrand as in Eq. (30). The procedure can be applied analogously by exchanging the roles of ξ and η.

Finally, the global two-dimensional quadrature rule is obtained by collecting the contributions from all subdomains Q_k.

The accuracy and computational cost of the adopted quadrature strategy are influenced by the local regularity of the zero level-set boundary. For smooth cutout boundaries, the procedure inherits the high-order accuracy of the underlying one-dimensional quadrature rules. More complex topologies, including multiple cutouts, boolean combinations of implicit functions, and intersecting boundaries, can also be treated within the level-set framework [64,65]. However, sharp corners, cusps, nearly touching cutouts, or junctions generated by intersecting cutouts may locally reduce the convergence rate and require increased quadrature order or additional recursive subdivision. Therefore, for such configurations, quadrature settings should be verified by monitoring the convergence of geometric quantities, such as the cut-domain area and low-order moments, and selected entries of the assembled stiffness and mass matrices. A quantitative verification of

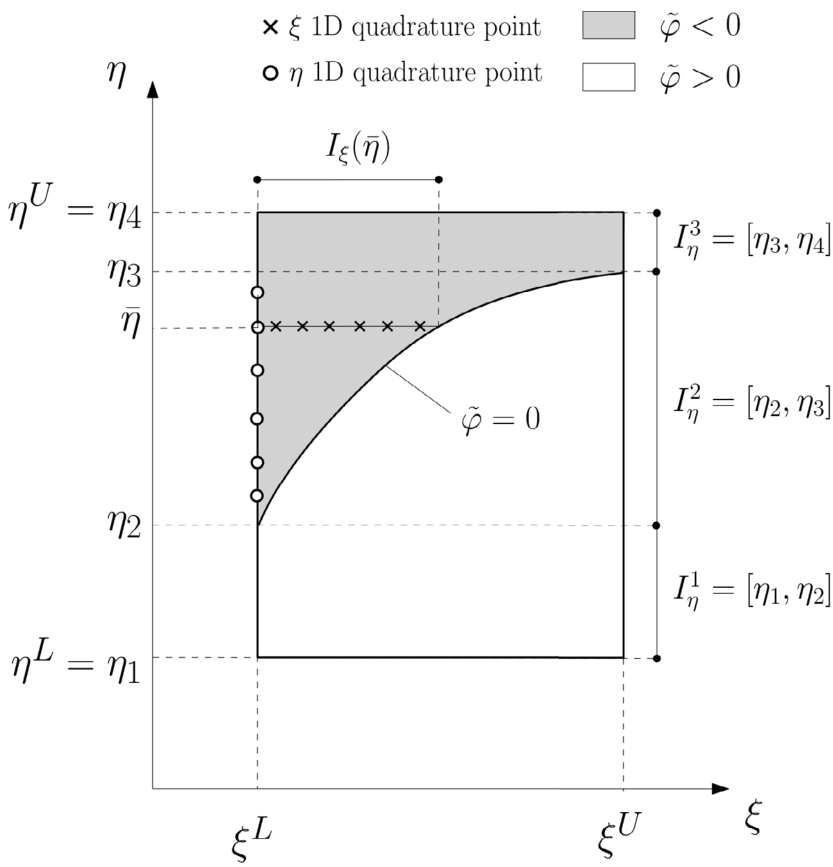

Fig. 3. Example of numerical integration over a subdomain Q_k intersected by the zero level set of $\tilde{\phi}$, illustrating the construction of the intervals I_η^i and $I_\xi(\eta)$ together with the corresponding one- and two-dimensional quadrature points.

the quadrature order adopted in the present analyses is reported in Section 4.1. It should be noted that the evaluation of the integral requires, at each quadrature point, the computation of the trial functions and their derivatives, as well as the laminate stiffness and inertia matrices. When the laminate fields are available in analytical form, the stiffness evaluation is straightforward. Otherwise, if the ply characteristics — namely material properties, thickness, and fibre orientation — are specified in discrete form, an appropriate interpolation procedure is required.

4. Results

The proposed formulation was implemented in an in-house code. Its numerical accuracy and convergence behaviour were first assessed through benchmark problems involving constant-stiffness and variable-stiffness cylindrical panels, with and without cutouts. Unless otherwise stated, the approximation introduced in Eq. (22) was constructed using the same number of Legendre-based trial functions for all primary variables, namely $M_\chi = N_\chi = N$. For integrations over level-set-defined cut domains, the order q of the one-dimensional Gauss rules employed in Saye's algorithm was initially set to $q = N + 1$, based on the polynomial exactness of Gauss quadrature and the degree of the Legendre-based products entering the structural operators. Its adequacy was subsequently checked at fixed approximation order by monitoring the domain area, selected stiffness and mass matrix entries, and representative natural frequencies, and q was increased whenever the monitored quantities had not yet reached convergence. In all the numerical applications, the energy-equivalent corrected transverse-shear constitutive matrix $\boldsymbol{A}_S^{\langle r \rangle}$ was evaluated locally at each integration point by implementing the Whitney–Pagano procedure exactly as described for laminated composite shell sections in the Abaqus® documentation [58]. Specifically, the reconstructed through-thickness shear-stress field was used to determine the energy-equivalent shear-flexibility matrix $\mathbf{F}_S^{\langle r \rangle}$, from which $\boldsymbol{A}_S^{\langle r \rangle} = \boldsymbol{F}_S^{\langle r \rangle\,-1}$ and $\mathbf{K}_S = \boldsymbol{A}_S^{\langle r \rangle} \mathbf{A}_{S,0}^{\langle r \rangle\,-1}$.

Following the convergence and validation assessment, the framework was applied to representative case studies demonstrating its modelling versatility and analysis capabilities. Unless otherwise stated, the finite element reference solutions generated in this work and used for validation were obtained with Abaqus® using four-node S4R reduced-integration shell elements. The finite element models were built on the panel mid-surface, with the same geometry, material properties, laminate stacking sequences, offsets, and boundary conditions as the corresponding analyses performed with the present framework. For variable-stiffness laminates, the curvilinear fibre paths were approximated by assigning constant element-wise material orientations evaluated at the element centroid from the prescribed orientation field. When spatially varying thickness distributions were considered, the thickness field was assigned element-wise from the same interpolated data used in the present formulation. Finite element mesh convergence was assessed through successive refinement, and the adopted discretization was selected when the maximum relative variation over the set of considered natural frequencies between successive meshes was of the order of 0.1%; at each refinement level, the prescribed continuous fibre-angle field was resampled at the element centroids.

4.1. Convergence and validation

The first benchmark problem concerns the free vibration response of fully clamped isotropic aluminium panels, for which reference solutions obtained by the generalized differential quadrature method [66] and the finite-strip method [67] are available in the literature. Square

Table 2
Convergence behaviour of the first four natural frequencies f [Hz] for flat and cylindrical ($R = 2$ m) fully clamped isotropic panels with and without a central square cutout.

	Mode	Without cutout (c = 0)				With central cutout (c = 0.25)			
		#1	#2	#3	#4	#1	#2	#3	#4
$R = \infty$	$N = 8$	69.72	142.21	142.21	209.67	127.30	165.13	165.13	221.40
	$N = 16$	69.72	142.17	142.17	209.59	126.85	151.08	151.08	208.98
	$N = 24$	69.72	142.17	142.17	209.59	126.75	149.33	149.33	205.79
	$N = 32$	69.72	142.17	142.17	209.59	126.70	148.70	148.71	204.94
	Ref. [66]	69.72	142.17	142.17	209.59	127.02	148.19	148.30	199.09
	Ref. [67]	70.28	144.27	144.67	214.82	128.21	151.01	152.37	209.99
	FEM*	69.77	142.52	142.57	210.05	126.66	147.77	147.77	198.86
$R = 2$ m	$N = 8$	215.05	244.69	328.25	336.38	223.77	238.57	321.15	348.07
	$N = 16$	214.83	244.17	327.85	335.99	189.39	194.96	297.59	319.03
	$N = 24$	214.83	244.17	327.85	335.99	183.82	187.96	294.66	309.39
	$N = 32$	214.83	244.17	327.85	335.99	183.74	187.64	294.66	309.08
	Ref. [66]	215.11	245.06	328.12	336.52	183.77	186.64	294.96	310.12
	Ref. [67]	219.04	250.71	330.62	339.79	198.95	203.37	305.13	329.26
	FEM*	215.04	245.02	328.06	336.48	183.62	186.36	294.52	308.79

From Ref. [66].

planform panels with side length $a = 0.5$ m and thickness $h = 2$ mm are analysed for two curvature conditions, namely a flat plate with $R = \infty$ and a cylindrical panel with radius $R = 2$ m. Both the intact configuration and the configuration with a centrally located square cutout of side length $c = 0.25$ m are considered. The aluminium material is characterized by Young's modulus $E = 68.796$ GPa, Poisson's ratio $\nu = 0.3$, and mass density $\rho = 2720$ kg/m^3.

Convergence with respect to the polynomial approximation order was assessed by comparing two successively enriched bases. Let $\omega_j^{(N)}$ denote the jth natural frequency computed using N Legendre polynomial terms in each parametric direction. The convergence indicator was defined as

$$\varepsilon_\omega(N) = \max_{j=1,\dots,n_\mathrm{m}} \frac{\left|\omega_j^{(N+\Delta N)} - \omega_j^{(N)}\right|}{\omega_j^{(N+\Delta N)}}, \tag{34}$$

where n_m is the number of monitored vibration modes and ΔN is the basis-enrichment increment, namely the increase in the number of Legendre polynomial terms in each parametric direction between two successive approximation levels. In the present analyses, $\Delta N = 8$. The approximation associated with N was considered converged when $\varepsilon_\omega(N) \leq 5 \times 10^{-3}$, corresponding to a maximum relative change of 0.5% after the subsequent basis enrichment. Mode correspondence between successive approximations was checked by comparing the associated mode shapes, particularly in the presence of closely spaced or repeated frequencies. Convergence results for increasing numbers of employed trial functions are reported in Table 2 monitoring the first four natural frequencies. For validation, the table also includes the available reference solutions and finite element predictions.

Table 2 confirms the convergence of the proposed framework for representative benchmark configurations. The intact panels exhibit rapid convergence as the polynomial basis is enriched, whereas configurations with cutouts require a larger basis because of the geometrical discontinuities introduced by the openings. According to the criterion defined in Eq. (34), $N = 24$ is sufficient for all the configurations considered in the table. The converged results show good agreement with the available reference and FEM solutions, supporting the accuracy of the adopted discretization strategy.

The stable convergence of the natural frequencies and associated mode shapes during basis enrichment provided the primary indication of numerical stability. At each approximation order, this assessment was complemented by checks of the symmetry of the discrete stiffness and mass matrices, the positive definiteness of the mass matrix, the residuals of the computed eigenpairs, and the absence of negative or spurious eigenvalues. No loss of numerical stability affecting the reported low-frequency modes was observed up to the largest value of N considered in the analyses. As an illustrative verification of the adopted quadrature setting, the flat fully clamped panel with the central square cutout was considered at the fixed Ritz approximation order $N = 24$, while the one-dimensional quadrature order q was increased from 4 to 48. The solution obtained using $q_\mathrm{ref} = 48$ was taken as the numerical reference, and the absolute relative error was evaluated as

$$\varepsilon_X(q) = \left|\frac{X^{(q)} - X^{(q_\mathrm{ref})}}{X^{(q_\mathrm{ref})}}\right|, \qquad X \in \{K^\star, M^\star, f_1, f_2, f_4\}. \tag{35}$$

The quantities $K^\star = K_{i^\star i^\star}$ and $M^\star = M_{i^\star i^\star}$ denote the diagonal stiffness and mass entries associated with the generalized coefficient of the highest-order transverse-displacement trial function. Owing to the symmetry of the benchmark configuration, the second and third frequencies are repeated, $f_2 = f_3$, and are therefore represented by a single convergence curve. The computed domain area was instead compared with its exact value. It is worth noting that the reference order $q_\mathrm{ref} = 48$ data are not shown because the corresponding relative errors vanish by definition.

As shown in Fig. 4, the exact domain area is recovered for all the quadrature orders considered, whereas the selected matrix entries and natural frequencies converge rapidly as q is increased. At $q = N + 1 = 25$, the errors in $K^\star$ and $M^\star$ are of order 10^{-10}, while the maximum error among the monitored frequencies is of order 10^{-7}. This behaviour is consistent with the polynomial structure of the Legendre-based integrands and supports the use of $q = N + 1$ as the initial quadrature order, subject to a convergence check for more demanding geometries or spatially varying fields.

A variable-stiffness laminated cylindrical panel with dimension $2L = a = 0.3$ m and varying radius R is analysed under simply-supported boundary conditions. The laminate is composed of variable angle tow (VAT) plies [68], in which the fibre orientation varies continuously along a prescribed baseline axis r defined on the panel mid-surface. With reference to Fig. 5, the fibre angle distribution is given by

$$\theta(r) = \phi + \theta_A + \frac{\theta_B - \theta_A}{r_B - r_A}\left(|r| - r_A\right), \tag{36}$$

where ϕ denotes the inclination of the baseline with respect to the x_1-axis while θ_A and θ_B are the fibre orientations at $r = r_A$ and $r = r_B$, respectively. The coordinate r is measured from the point O', defined as the orthogonal projection of the panel centre onto the baseline. The notation $\theta_0 + \langle\theta_A \mid \theta_B\rangle$ is adopted to identify the ply fibre path, with angles expressed in degrees.

The stacking sequences considered belong to the family $[90 + \langle 0 \mid \theta_B\rangle/90 - \langle 0 \mid \theta_B\rangle/90 + \langle 0 \mid \theta_B\rangle/90 - \langle 0 \mid \theta_B\rangle]_S = \left[90 \pm \langle 0 \mid \theta_B\rangle\right]_{2S}$, with the VAT ply baseline aligned with the panel generators and parameters $r_A = 0$ and $r_B = L$. Each lamina has thickness $t = 1.31 \times 10^{-4}$ m and material properties $E_1 = 163$ GPa, $E_2 = 10$ GPa,

Table 3
Normalized fundamental frequency, $\tilde{\omega}$ for $[90 \pm \langle 0 \mid \theta_B \rangle]_{2S}$ cylindrical panels with different radii.

a/R	$\theta_B = 0$			$\theta_B = 30$			$\theta_B = 60$		
	FEM	Present	%error	FEM	Present	%error	FEM	Present	%error
0	2.027	2.021	−0.32%	2.268	2.249	−0.83%	2.438	2.411	−1.12%
0.05	2.304	2.297	−0.31%	2.705	2.682	−0.86%	2.848	2.815	−1.16%
0.075	2.604	2.595	−0.35%	3.136	3.105	−0.98%	3.210	3.169	−1.29%
0.1	2.971	2.954	−0.55%	3.631	3.579	−1.43%	3.597	3.535	−1.72%
0.2	4.692	4.626	−1.42%	5.656	5.498	−2.79%	5.019	4.886	−2.66%

Table 4
Normalized fundamental frequency, $\tilde{\omega}$ for $[90 \pm \langle 0 \mid \theta_B \rangle]_{2S}$ cylindrical panels with different radii and central circular cutouts of different diameters.

D/a	a/R	$\theta_B = 0$			$\theta_B = 30$			$\theta_B = 60$		
		FEM	Present	%error	FEM	Present	%error	FEM	Present	%error
0.2	0	1.857	1.856	−0.05%	2.118	2.103	−0.69%	2.322	2.297	−1.09%
	0.05	2.191	2.190	−0.07%	2.634	2.615	−0.73%	2.790	2.762	−1.03%
	0.075	2.539	2.535	−0.14%	3.122	3.095	−0.87%	3.204	3.167	−1.16%
	0.1	2.948	2.940	−0.28%	3.655	3.615	−1.09%	3.627	3.577	−1.37%
	0.2	4.811	4.748	−1.32%	5.807	5.650	−2.70%	5.158	5.021	−2.66%
0.4	0	1.737	1.734	−0.20%	2.182	2.158	−1.12%	2.539	2.501	−1.50%
	0.05	2.195	2.191	−0.17%	2.795	2.767	−0.97%	2.895	2.855	−1.37%
	0.075	2.634	2.628	−0.23%	3.345	3.311	−1.01%	3.261	3.217	−1.35%
	0.1	3.117	3.106	−0.34%	3.915	3.870	−1.16%	3.679	3.626	−1.42%
	0.2	4.986	4.939	−0.95%	5.804	5.744	−1.05%	5.329	5.205	−2.32%
0.6	0	1.871	1.865	−0.32%	2.821	2.772	−1.72%	3.452	3.380	−2.11%
	0.05	2.495	2.485	−0.40%	3.344	3.298	−1.37%	3.626	3.553	−2.03%
	0.075	3.012	3.003	−0.31%	3.812	3.766	−1.20%	3.826	3.752	−1.94%
	0.1	3.499	3.486	−0.38%	4.265	4.218	−1.11%	4.080	4.004	−1.87%
	0.2	4.589	4.569	−0.44%	5.335	5.289	−0.86%	5.313	5.211	−1.92%

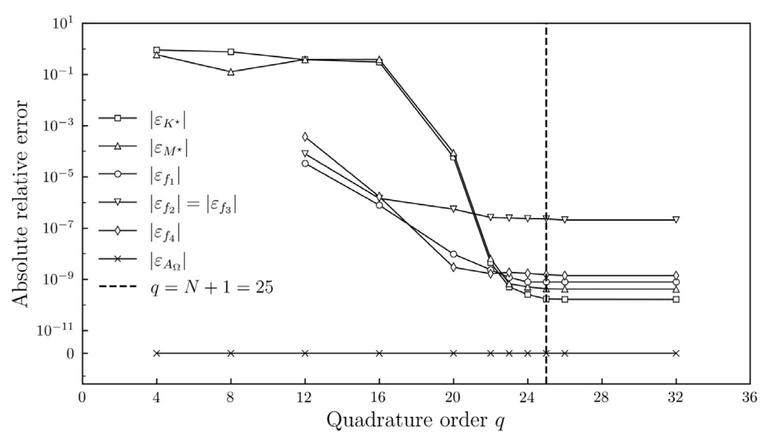

Fig. 4. Illustrative quadrature-convergence analysis for the flat fully clamped panel with a central square cutout at $N = 24$. Absolute relative errors in the domain area, $K^\star$, $M^\star$, and the monitored natural frequencies are reported. The dashed line denotes the adopted integration order $q = N + 1 = 25$.

$G_{12} = G_{13} = G_{23} = 5$ GPa, $\nu_{12} = 0.3$, and density $\rho = 1480$ kg/m^3. The total laminate thickness is $h = 1.048 \times 10^{-3}$ m.

Free vibration analyses are first performed for the uncut configuration. The results are compared with finite element reference solutions generated according to the modelling strategy described above. The corresponding finite element models comprise approximately 60,000 degrees of freedom. It is worth noting that such FE models entail a significantly higher preprocessing effort, particularly for configurations involving complex geometries. Table 3 reports the normalized fundamental frequency, $\tilde{\omega} = \frac{\omega}{2\pi} \frac{L^2}{h} \sqrt{\frac{\rho}{E_2}}$, together with a comparison against the corresponding finite element results for panels with varying radius R.

The close agreement observed across all test cases, with discrepancies consistently below 3%, supports the accuracy of the proposed approach. Minor deviations are observed, becoming more pronounced for smaller radii and increasing values of θ_B, corresponding to more strongly curved fibre paths.

Further validation is presented in Table 4, which reports results for the same panels incorporating a central circular cutout with diameter ratios $D/a = 0.2$, 0.4, and 0.6. In this case, the analyses indicate the need for a higher-order Ritz approximation to achieve convergence. Specifically, the reported results are obtained using trial functions constructed with 32 polynomial terms, which are sufficient to ensure converged solutions. Also in this case, very good agreement is observed with the FE reference solutions. The corresponding finite element models comprise approximately 60,000 degrees of freedom, and the observed trends and discrepancies are consistent with those discussed for the uncut configuration.

The small discrepancies observed with respect to the finite element results are consistent with the different numerical representations adopted by the two approaches. In the proposed formulation, the shell geometry, curvilinear fibre paths, and cutout boundaries are described analytically, and the governing equations are solved within

Table 5
First six normalized natural frequencies $\tilde{\omega}$ for fully clamped isotropic panels with five-pointed and eight-pointed star-shaped cutouts: comparison between the present solution and FEM results.

	Mode #	$R=\infty$			R=1.5		
		Present	FEM	%error	Present	FEM	%error
Five-pointed star	1	1.838	1.836	0.14%	4.721	4.712	0.20%
	2	3.225	3.172	1.68%	6.313	6.188	2.01%
	3	3.226	3.172	1.70%	6.606	6.516	1.38%
	4	4.966	4.961	0.10%	6.746	6.609	2.07%
	5	5.952	5.916	0.61%	7.562	7.403	2.15%
	6	7.402	7.263	1.92%	9.438	9.328	1.18%
Eight-pointed star	1	1.822	1.817	0.28%	4.309	4.300	0.23%
	2	3.127	3.088	1.28%	5.552	5.500	0.93%
	3	3.127	3.088	1.26%	5.908	5.845	1.08%
	4	4.938	4.900	0.77%	5.982	5.886	1.64%
	5	5.853	5.798	0.93%	6.722	6.648	1.12%
	6	7.371	7.218	2.12%	8.316	8.254	0.74%

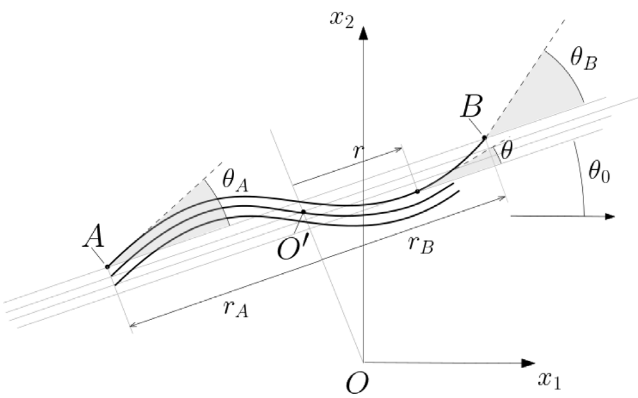

Fig. 5. Definition of variable angle tow (VAT) fibre paths parameters.

a global approximation framework. By contrast, the finite element reference solution relies on a mesh-based discretization, in which the cylindrical geometry is represented over a finite-element mesh and the continuously varying fibre orientations are approximated through element-wise constant fibre orientations. Residual cross-discretization differences may become more pronounced for configurations involving smaller radii, strongly curved fibre paths, and geometric discontinuities introduced by cutouts, where the structural response is more sensitive to local stiffness variations.

To further assess the applicability of the proposed level-set-based quadrature strategy to non-convex cutout geometries, fully clamped isotropic panels with dimensions $2L = a = 0.3$ m and thickness $h = 1.048 \times 10^{-3}$ m are considered. Two curvature conditions are analysed, namely a flat plate with $R = \infty$ and a cylindrical panel with $R = 1.5$ m. Each configuration contains a centrally located star-shaped cutout, defined either by a five-pointed or an eight-pointed boundary with mean radius $\bar{r} = 0.035$ m. The level-set functions used to describe these geometries are reported in Appendix A. The material is taken as aluminium, with Young's modulus $E = 72.24$ GPa, Poisson's ratio $\nu = 0.33$, and mass density $\rho = 2700$ kg/m^3. These non-convex geometries provide a more demanding test for the integration procedure because their boundaries include alternating concave and convex portions. The approximation order $N = 32$ was selected according to the criterion defined in Eq. (34) using the prescribed convergence threshold of 0.5%. The first six normalized natural frequencies $\tilde{\omega}$ are reported in Table 5 and compared with converged finite element solutions generated according to the modelling strategy described above. The corresponding finite element models comprise 181,371 and 151,770 degrees of freedom for the five-pointed and eight-pointed star-shaped cutouts, respectively. The agreement obtained for both star-shaped geometries provides further evidence of the capability of the proposed formulation to accurately handle non-convex cutout boundaries within the level-set-based integration framework.

Overall, these findings validate both the correctness of the implementation and the effectiveness of the proposed approach for the free vibration analysis of variable-stiffness composite cylindrical panels, including configurations with geometric discontinuities. The finite element comparisons reported in the validation studies above also illustrate the compactness of the proposed algebraic model. When the same number N of Legendre polynomial terms is adopted for the construction of the trial functions of all five primary variables, the Ritz approximation contains $5N^2$ generalized unknowns; hence, the approximations with $N = 24$ and $N = 32$ used in the validation examples involve 2880 and 5120 unknowns, respectively. The corresponding finite element models, whose degrees of freedom are reported in the individual examples, lead to substantially larger algebraic systems.

This comparison provides quantitative evidence of the compactness of the global approximation adopted in the proposed framework. In addition, the implicit level-set description of cutout geometries reduces the geometry-preprocessing effort by avoiding the construction of boundary-fitted finite element meshes.

4.2. Example 1 - variable thickness plate with multiple cutouts

Let us consider an isotropic plate with spatially varying thickness and multiple geometric cutouts, whose configuration and reference dimensions are illustrated in Fig. 6(a). The thickness varies within the range $h_{\min} = 2.5$ mm to $h_{\max} = 10.0$ mm, exhibiting a highly non-uniform spatial distribution characterized by smooth gradients as well as localized discontinuities, as shown in the thickness map in Fig. 6(b).

The material is assumed to be homogeneous and isotropic, with properties representative of aluminium: Young's modulus $E = 72.24$ GPa, Poisson's ratio $\nu = 0.33$, and mass density $\rho = 2700$ kg/m^3. The plate is clamped along two opposite edges, as illustrated in Fig. 6(a).

The computational model is formulated by initially considering a cylindrical panel with radius $R \to \infty$, which degenerates to a flat plate configuration. The geometry is subsequently modified by introducing circular cutouts at two opposite corners, together with a central cutout defined through the boolean combination of a square and a circular shape (see Appendix A for the corresponding level-set definitions). For numerical implementation, the thickness field is sampled on a 401×401 grid of equally spaced control points and reconstructed via piecewise linear interpolation over scattered data; the thickness

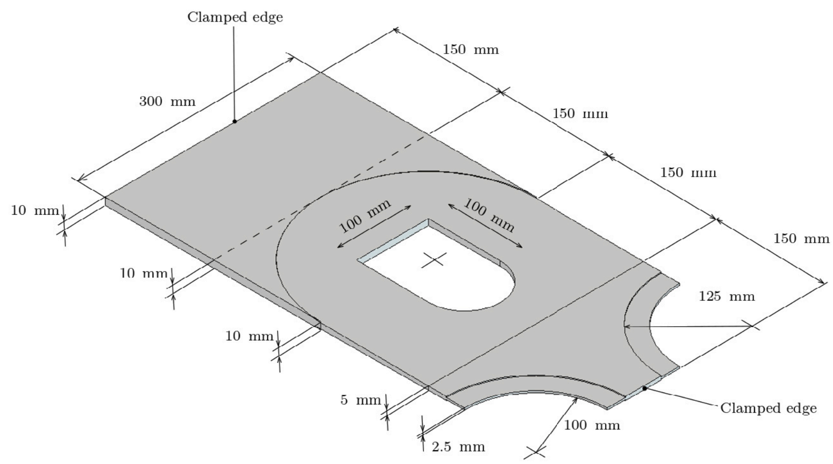

(a) Geometry of the variable-thickness aluminium plate.

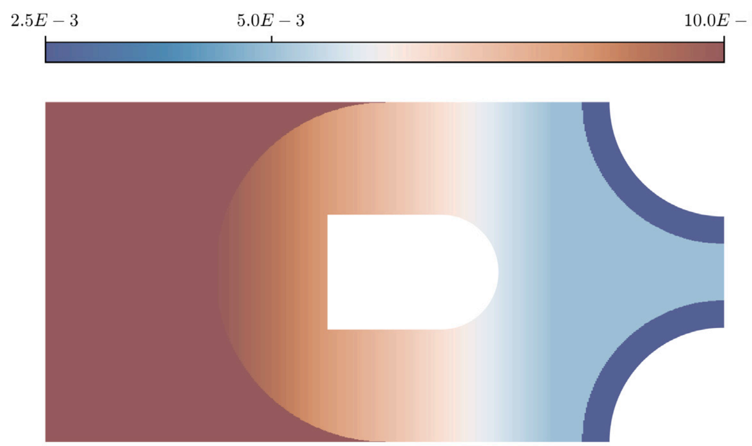

(b) Spatial distribution of the plate thickness.

Fig. 6. Geometrical description of the variable-thickness plate.

Table 6
Natural frequencies $f = \omega/(2\pi)$ [Hz] of the isotropic variable thickness flat plate.

Mode	1	2	3	4	5	6	7	8	9
FEM	94.28	135.65	244.73	323.71	444.11	514.77	611.63	738.46	887.80
Present	94.32	136.28	245.58	320.70	444.04	511.84	610.68	736.25	879.33
% error	0.04%	0.47%	0.34%	−0.93%	−0.01%	−0.57%	−0.16%	−0.30%	−0.95%

field data are also provided as Supplementary Data. Application of the convergence criterion defined in Eq. (34) to the first $n_{\mathrm{m}} = 9$ natural frequencies showed that trial functions constructed using $M_\chi = N_\chi = 24$ satisfied the prescribed convergence tolerance. The natural frequencies of the panel, $f = \omega/(2\pi)$, computed using the proposed framework, are reported in Table 6. For validation purposes, the results are compared with finite element reference solutions generated according to the modelling strategy described above; the corresponding FE model comprises approximately 684,546 degrees of freedom.

Excellent agreement is observed, with maximum discrepancies below 1%, thereby confirming the accuracy of the proposed formulation. The corresponding vibration mode shapes are illustrated in Fig. 7 and exhibit close agreement with those obtained from the finite element model.

4.3. Example 2 - parametric investigation of VAT cylindrical panels

The proposed framework enables parametric investigations of the free vibration response of variable-stiffness cylindrical panels. In particular, it supports systematic assessment of the influence of fibre steering on the structural dynamic behaviour, thereby providing valuable guidance for the identification and optimization of efficient design configurations for uncut and cut panels. To demonstrate these capabilities, the natural frequencies of a simply-supported, VAT laminated cylindrical panel with dimensions $2L = a = 0.3$ m and radius $R = 1.5$ m are evaluated for the laminate stacking sequence $\left[90 \pm \langle \theta_A | \theta_B \rangle\right]_{2S}$ as functions of the VAT fibre-path parameters. Both the intact configuration and a panel with a centrally located circular cutout, characterized by a diameter ratio $D/a = 0.4$, are considered. The results reported in the following are obtained with trial functions constructed using 24 Legendre polynomials in each parametric direction ($M_\chi = N_\chi = 24$) which yields converged solutions for the problem under consideration.

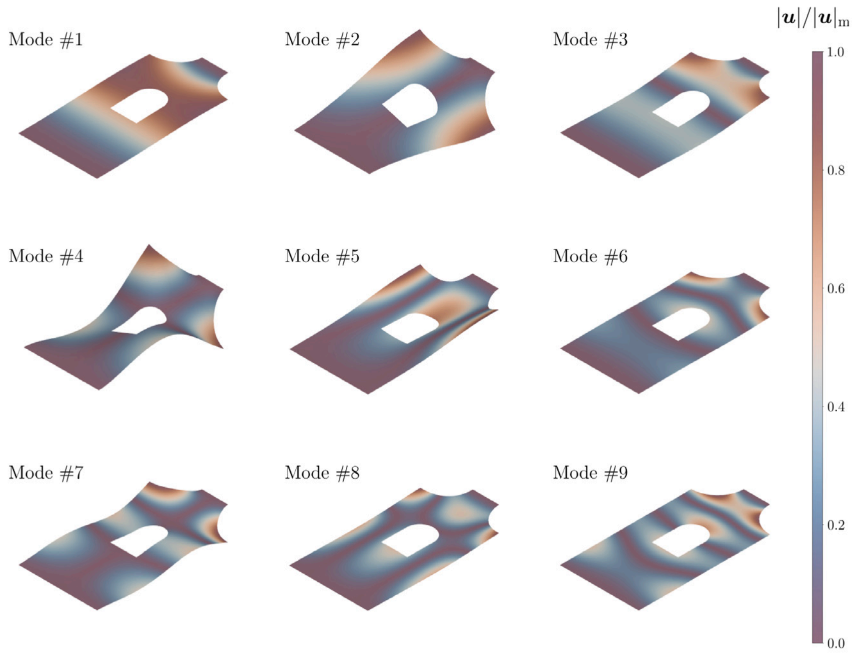

(a) Present solution.

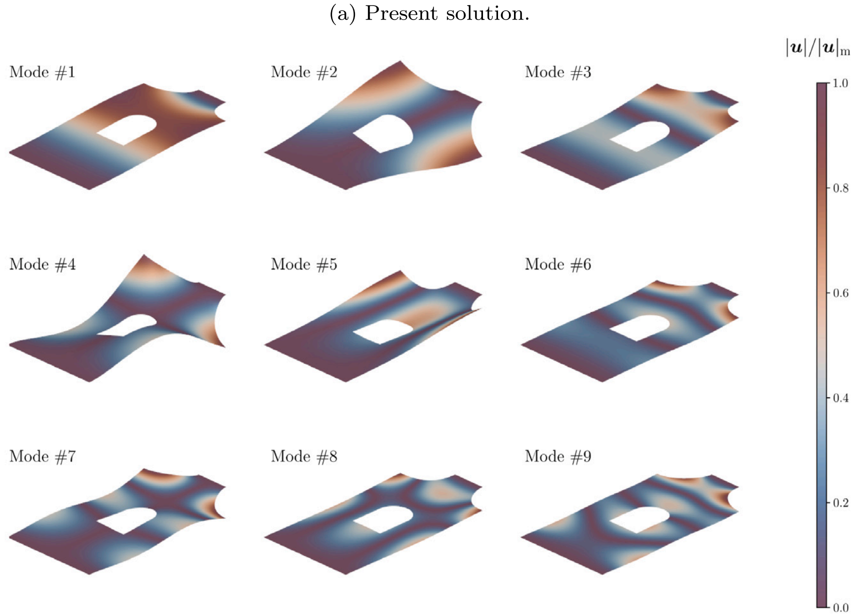

(b) FEM solution.

Fig. 7. Comparison of the first nine vibration mode shapes of the isotropic variable-thickness flat panel with cutouts: (a) present solution and (b) FEM solution. The colour scale denotes the normalized displacement magnitude.

Fig. 8 illustrates the variation of the nondimensional frequencies of the first two natural vibration modes as functions of the characteristic VAT lamination angles. For both intact panels and panels with cutouts, the adoption of tailored fibre paths induces significant changes in the natural frequencies, thereby enabling effective tuning relative to conventional straight-fibre configurations. While the presence of the cutout markedly influences the absolute values of the natural frequencies, it does not compromise the ability to tailor the dynamic response through fibre steering.

Figs. 9 and 10 depict the first two mode shapes of the $[90\pm\langle\theta_A|\theta_B\rangle]_{2S}$ VAT panel for representative values of θ_A and θ_B.

The results reveal that variations in fibre paths not only modify the natural frequencies but also alter the corresponding modal characteristics. In particular, changes in the fibre orientation can lead, in certain cases, to a mode-shape exchange between the first and second vibration modes.

4.4. Example 3 — variable-stiffness cylindrical panel with reinforcement and multiple cutouts

The present application is intended to demonstrate the capability of the proposed approach in handling complex variable-stiffness panel configurations in the presence of multiple cutouts. To this end, the

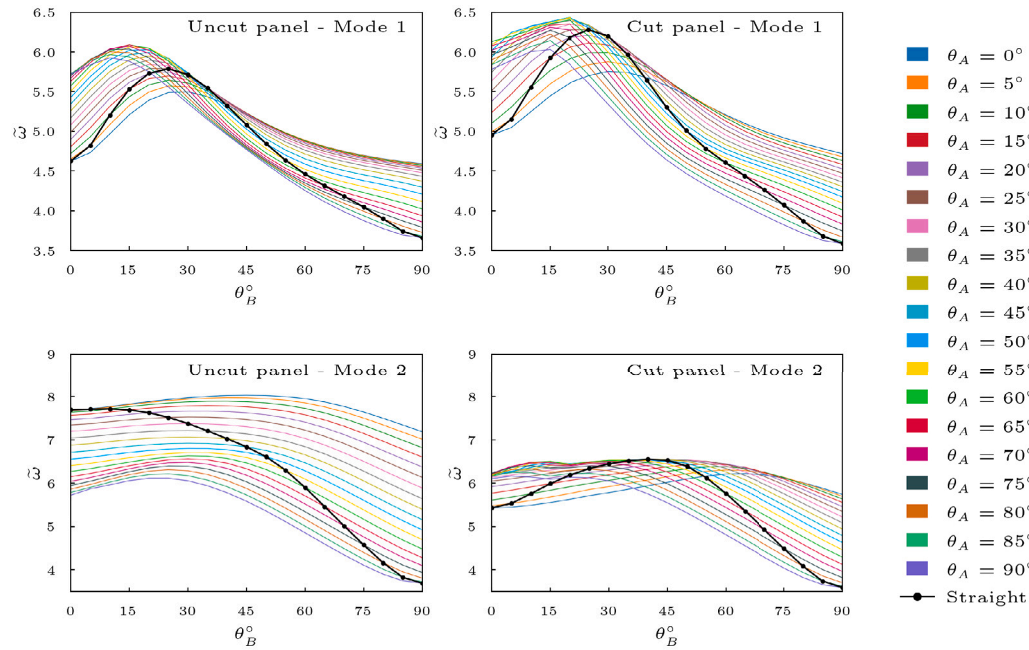

Fig. 8. Variation of the first two nondimensional natural frequencies of the $[90 \pm \langle\theta_A|\theta_B\rangle]_{2S}$ panel as functions of θ_B for different values of θ_A, for uncut and cut configurations.

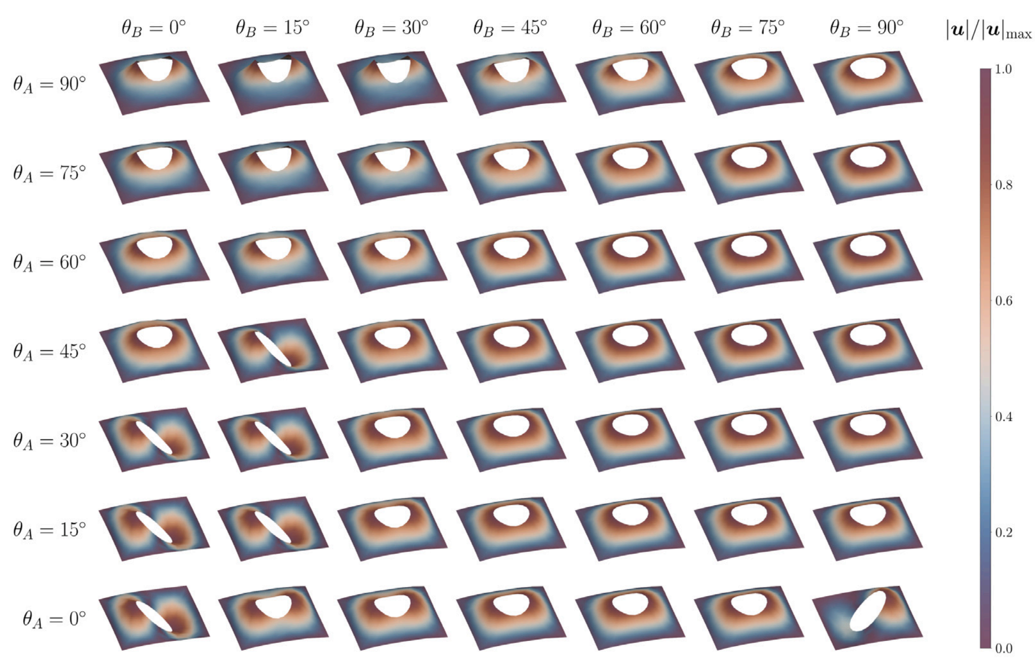

Fig. 9. First vibration mode shape of the $[90 \pm \langle\theta_A|\theta_B\rangle]_{2S}$ VAT cylindrical panel for selected fibre-path configurations.

cylindrical panel shown in Fig. 11(a) is considered, with radius R = 1.5 m, subtended angle $2\alpha = 12°$, length $2L = 0.6$ m and thickness $t_s = 8$ mm. The panel is reinforced by three circumferential strips that symmetrically divide it into two bays; each strip has width w = 0.03 m and thickness $t_r = 12$ mm. Each bay contains a centrally located rectangular cutout with height $a = 0.15$ m, width $b = 0.1$ m and fillet radius $r = 0.025$ m; the cutout geometry is represented using superelliptic level-set functions. Simply supported boundary conditions are imposed along all external edges of the panel.

The panel skin is constructed from variable-stiffness plies whose curvilinear fibre-angle maps were generated from a two-dimensional irrotational flow field represented by a velocity potential ϕ satisfying Laplace's equation over the panel planform excluding the cutouts. A uniform free-stream direction, coincident with the prescribed asymptotic fibre orientation, was imposed at the external boundary, while the cutout boundaries were treated as impermeable. Numerically, the corresponding harmonic-streamfunction formulation was solved using a finite-difference scheme on a regular grid, and the local lamination angle θ was determined from the direction of the resulting velocity field. For the asymptotic fibre directions $\theta = -45°,\ 0°,\ 45°,\ 90°$, Fig. 12 shows the planform projections of the corresponding lamination-angle distributions, measured with respect to the circumferential direction,

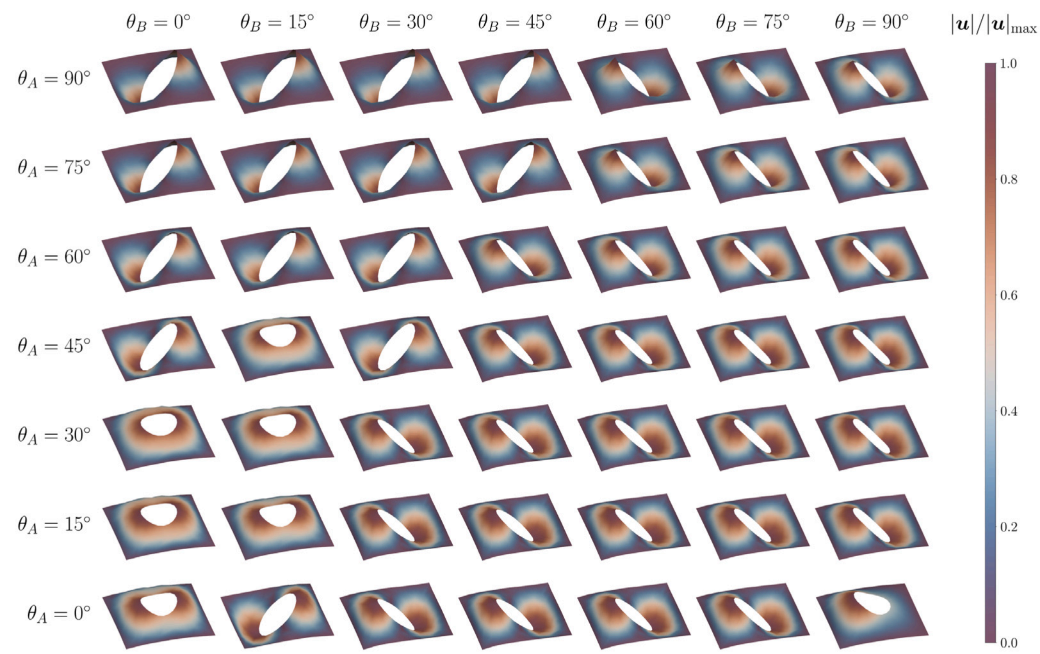

Fig. 10. Second vibration mode shape of the $\left[90 \pm \langle \theta_A | \theta_B \rangle\right]_{2S}$ VAT cylindrical panel for selected fibre-path configurations.

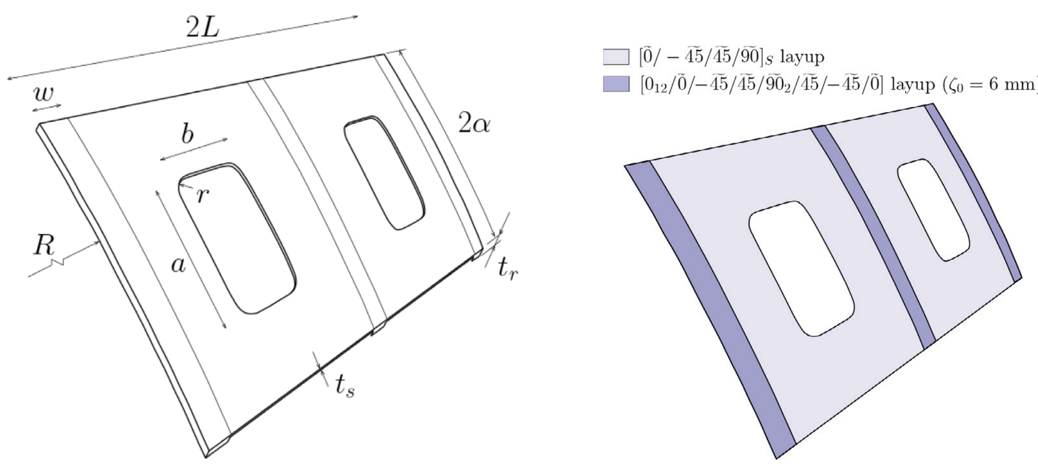

(a) Geometrical scheme.

(b) Modelling scheme

Fig. 11. Panel with two symmetric cutouts and three reinforcing strips.

together with the associated fibre paths. The latter are contour lines of the computed streamfunction and are included for visualization purposes. The complete lamination-angle maps used in the analysis are provided as Supplementary Data. Each map is represented on a 75×100 grid of equally spaced control points with the local angles reconstructed by piecewise-cubic interpolation of the control-point data. Within the stacking sequence notation, plies characterized by such curvilinear fibre paths are denoted by $\widetilde{\theta}$, whereas θ refers to conventional plies with straight fibres oriented at a constant angle.

It is emphasized that no manufacturing or technological constraints are imposed on the fibre paths in the present study. This assumption is adopted deliberately to isolate and assess the modelling capabilities of the proposed framework for general variable-stiffness laminates. The numerical admissibility of general prescribed fibre paths should not be interpreted as evidence of their practical manufacturability, which may be limited by constraints associated with the fibre-deposition process such as minimum steering radius, tow-continuity requirements, gap/overlap formation, and manufacturing-induced defects. Accordingly, the panel skin layup is defined as $[\widetilde{0}/-\widetilde{45}/\widetilde{45}/\widetilde{90}]_S$, whereas the reinforcing strips are constructed using a $[0_{12}]$ layup with circumferentially oriented fibres. The material properties adopted for both the skin and the reinforcing plies are identical to those used in the previous example, and the ply thickness is set to $t_p = 1.0$ mm.

As illustrated in Fig. 11(b), the single-domain structural model is formulated by partitioning the panel into five regions: three corresponding to the reinforcing strips and two associated with the inter-strip skin. The inter-strip regions are assigned the variable-stiffness layup $[\widetilde{0}/-\widetilde{45}/\widetilde{45}/\widetilde{90}]_S$, while the strip regions are modelled using the composite layup $[0_{12}/\widetilde{0}/-\widetilde{45}/\widetilde{45}/\widetilde{90}/\widetilde{90}/\widetilde{45}/-\widetilde{45}/\widetilde{0}]$, obtained by superimposing the skin and reinforcement contributions; to account for

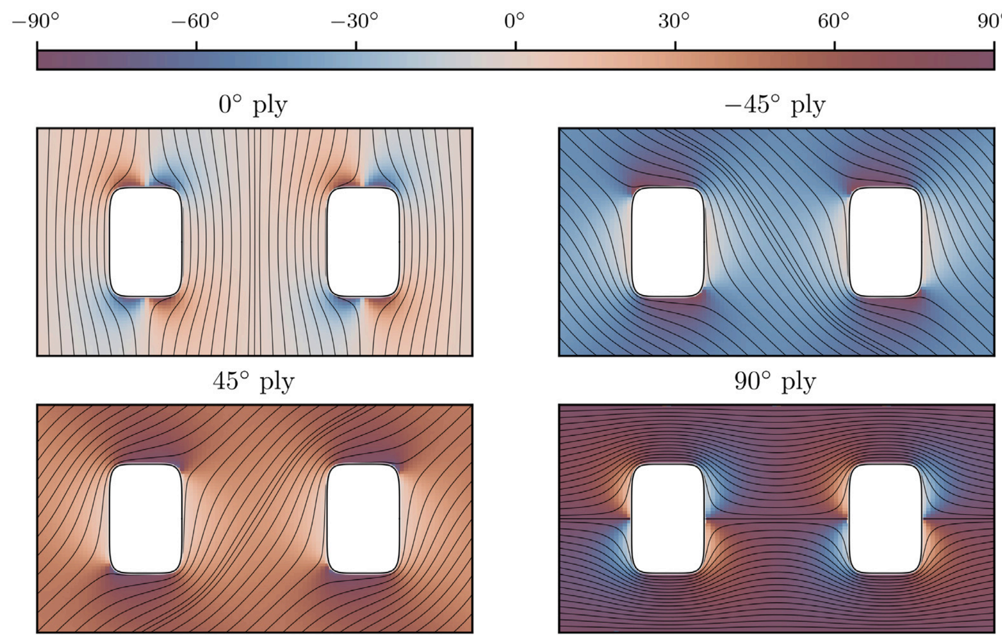

Fig. 12. Planform projection of the ply lamination angle distribution and corresponding fibre trajectories for different values of the asymptotic angle θ.

Table 7
Natural frequencies $f = \omega/(2\pi)$ [Hz] of the cylindrical panel with two superelliptical cutouts and stiffening strips: comparison between present and FEM results for constant-stiffness and variable-stiffness configurations.

Mode	Constant stiffness			Variable stiffness		
	Present	FEM	%error	Present	FEM	%error
1	737.42	737.34	0.01%	777.23	774.60	0.34%
2	848.09	841.67	0.76%	899.20	891.39	0.88%
3	980.73	976.77	0.41%	1018.79	1012.41	0.63%
4	1132.96	1128.96	0.35%	1165.92	1158.97	0.60%
5	1280.25	1275.48	0.37%	1284.55	1276.77	0.61%
6	1293.15	1287.58	0.43%	1302.23	1292.41	0.76%

the eccentricity of the reinforcing strips with respect to the reference mid-surface, an offset $\zeta_0 = 6.0$ mm is introduced for the corresponding regions.

For validation and accuracy assessment, results for the same panel built with straight-fibre composites are also reported. In particular, a symmetric laminate stacking sequence $[0/-45/45/90]_S$ is considered for the skin and a $[0_{13}/-45/45/90/90/45/-45/0]$ layup is considered for the strip regions where the $\zeta_0 = 6.0$ mm offset is set.

Table 7 reports the first six natural frequencies $f = \omega/(2\pi)$ of the panel, obtained using the proposed framework with trial functions constructed using 32 Legendre polynomials in each parametric direction, i.e. $M_\chi = N_\chi = 32$. This approximation order satisfies the convergence criterion defined in Eq. (34). For both the straight-fibre and variable-stiffness configurations, the predicted natural frequencies are compared with corresponding finite element results. The finite element model used for this comparison comprises 218,286 degrees of freedom. A very good agreement is observed, with discrepancies consistently below 1%. This level of accuracy substantiates the robustness of the proposed framework and provides a reliable basis for its application to configurations involving curvilinear fibre paths.

To complete the presentation of the results for the investigated panel, Fig. 13 illustrates the vibration modes, highlighting the deformation patterns induced by the presence of cutouts, reinforcements, and variable-stiffness effects.

Focusing on the variable-stiffness configuration with curvilinear fibre paths, the results highlight the pronounced influence of spatially varying fibre orientations on the dynamic response of the structure. In particular, for the considered fibre trajectories and layup, an increase in the natural frequencies is observed. It is worth noting that the proposed material configuration is not derived from an optimization process — being beyond the scope of the present work — but is instead adopted as a representative example to demonstrate the capabilities of the proposed framework.

Overall, these findings demonstrate the capability of the proposed framework to quantify the influence of variable-stiffness design on the dynamic characteristics of composite cylindrical panels and to support the assessment of different fibre-path configurations. For the configuration considered in this example, the variable-stiffness layup increases the first six natural frequencies by approximately 0.34%–6.03% relative to the corresponding straight-fibre configuration, depending on the vibration mode. It should be emphasized that the increases in natural frequency observed in the present study are specific to the fibre trajectories, laminate configurations, cutout geometries, boundary conditions, and reinforcement layouts examined. Accordingly, they should not be interpreted as generally applicable design rules. Establishing broader and more robust trends will require systematic parametric and optimization studies spanning a wider range of structural configurations.

5. Conclusions

A unified computational framework has been developed for the free vibration analysis of composite laminated cylindrical panels with cutouts. The proposed approach enables the single-domain treatment of cylindrical panels with complex cutout geometries while simultaneously accommodating variable-stiffness laminates, non-uniform thickness distributions, and multi-region configurations. By combining geometry-independent global approximations, implicit geometric descriptions, and high-order quadrature techniques, the proposed formulation provides a unified, versatile, and algebraically compact analysis setting for geometrically and materially complex structures, while retaining a single global displacement approximation and avoiding independent subdomain fields and interface continuity constraints.

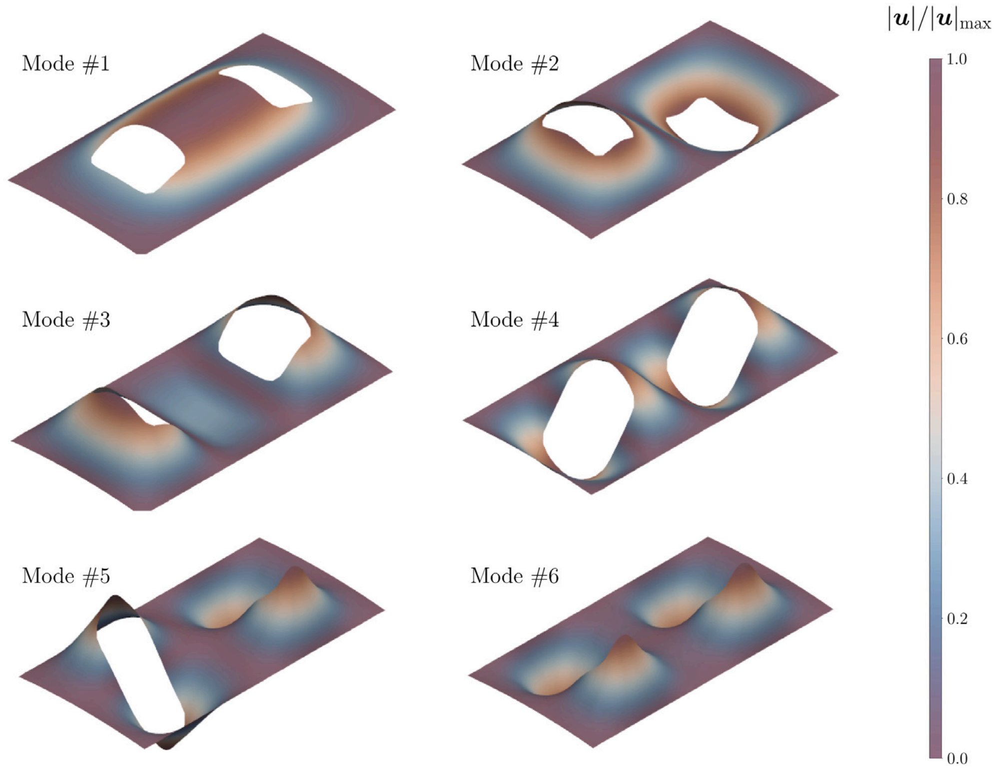

Fig. 13. Representative vibration mode shapes of the cylindrical panel with cutouts and reinforcing strips.

The framework has been validated against high-fidelity finite element simulations, showing close agreement with reference solutions across a range of benchmark configurations. The results confirm its ability to accurately capture the coupled effects of curvature, material anisotropy, spatial stiffness variations, and geometric discontinuities. The application studies further demonstrate the capability of the proposed approach to quantify the combined influence of stiffness variability, cutout geometry, non-uniform thickness, and local reinforcement on the dynamic response of composite cylindrical panels. For the configurations examined, the results show that stiffness tailoring through spatially varying fibre orientations can be used to modulate the natural frequencies. The presented findings are specific to the geometries, laminate configurations, fibre trajectories, boundary conditions, reinforcement layouts, and vibration modes considered herein and should not be interpreted as general design guidelines. The versatility of the proposed formulation opens the way to several future developments and engineering applications. These include systematic parametric and sensitivity studies, the construction of quantitative design maps, and optimization procedures involving fibre trajectories, thickness distributions, cutout geometries, and reinforcement layouts. One possible application, among several, is the minimization of structural mass subject to prescribed lower bounds on selected natural frequencies, with fibre-path parameters and local thickness distributions treated as design variables. Alternative objectives may include the maximization of selected natural frequencies, modal separation, prescribed frequency placement, or the recovery of vibration performance degraded by the presence of cutouts.

Declaration of competing interest

The authors declare that they have no known competing financial interests or personal relationships that could have appeared to influence the work reported in this paper.

Acknowledgements

The author acknowledges the support from the Space It Up! project funded by the Italian Space Agency, ASI, and the Ministry of University and Research, MUR, under contract no. 2024-5-E.0 - CUP n. I53D24000060005.

Appendix A. Level-set functions for the cutouts

Level-set functions for circular, elliptical, rectangular, superelliptical and star-shaped cutout shapes are reported as examples, with reference to the geometrical parameters shown in Fig. A.1.

– circular shape

$$\varphi_1(x_{1c}, x_{2c}, r) = 1 - \left(\frac{x_1 - x_{1c}}{r}\right)^2 - \left(\frac{x_2 - x_{2c}}{r}\right)^2 \tag{A.1}$$

– elliptical shape

$$\varphi_2(x_{1c}, x_{2c}, a, b, \beta) = 1 - \left(\frac{\tilde{x}_1}{a}\right)^2 - \left(\frac{\tilde{x}_2}{b}\right)^2 \tag{A.2}$$

– rectangular shape

$$\varphi_3(x_{1c}, x_{2c}, w, h, \beta) = 1 - \left|\frac{\tilde{x}_1}{w} - \frac{\tilde{x}_2}{h}\right| - \left|\frac{\tilde{x}_1}{w} + \frac{\tilde{x}_2}{h}\right| \tag{A.3}$$

– superelliptical shape ($d > 1$)

$$\varphi_4(x_{1c}, x_{2c}, a, b, d, \beta) = 1 - \left(\frac{2\tilde{x}_1}{a}\right)^{2d} - \left(\frac{2\tilde{x}_2}{b}\right)^{2d} \tag{A.4}$$

– n-pointed star shape with mean radius $\bar{r}$

$$\varphi_5(x_{1c}, x_{2c}, \bar{r}, n, \beta) = \frac{\bar{r}^2}{\left[\cos^{10}\left(\frac{n}{4}\psi\right) + \sin^{10}\left(\frac{n}{4}\psi\right)\right]^{1/3}} - \tilde{x}_1^2 - \tilde{x}_2^2, \tag{A.5}$$

where $\psi = \mathrm{atan2}(\tilde{x}_2, \tilde{x}_1)$.

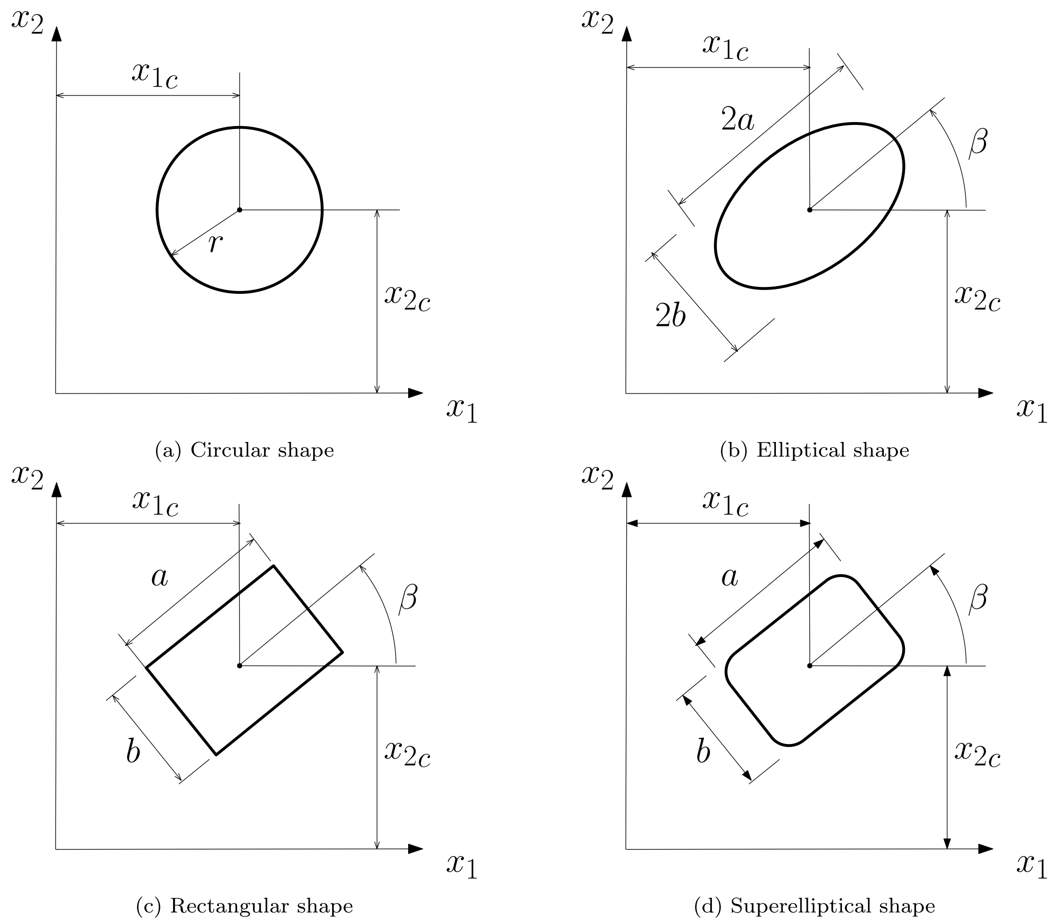

Fig. A.1. Geometrical parameters for simple geometry cutouts.

In the preceding equations one sets

$$\tilde{x}_1 = (x_1 - x_{1c})\cos\beta + (x_2 - x_{2c})\sin\beta \tag{A.6a}$$

$$\tilde{x}_2 = -(x_1 - x_{1c})\sin\beta + (x_2 - x_{2c})\cos\beta \tag{A.6b}$$

The level set functions for more complex cutout shapes or multiple cutouts can be obtained by combining the level set functions of simple shapes. In particular the level set function φ for the geometrical shape obtained by the union of multiple cutouts, each defined by the level set φ_i can be obtained as

$$\varphi = \sum_i \left[\max\left(0, 1 + \frac{\varphi_i}{\delta_1}\right)\right]^{\delta_2} - 1 \tag{A.7}$$

where the parameters δ_1 and δ_2 are suitably chosen [69].

Appendix B. Supplementary data

Supplementary material related to this article can be found online at https://doi.org/10.1016/j.tws.2026.115553.

Data availability

The numerical datasets supporting the findings of this study are available in the Supplementary Material associated with this article.

References

[1] B. Sobhani Aragh, E. Borzabadi Farahani, B. Xu, H. Ghasemnejad, W. Mansur, Manufacturable insight into modelling and design considerations in fibre-steered composite laminates: State of the art and perspective, Comput. Methods Appl. Mech. Engrg. 379 (2021) 113752, http://dx.doi.org/10.1016/j.cma.2021.113752.

[2] Y. Xu, J. Zhu, Z. Wu, Y. Cao, Y. Zhao, W. Zhang, A review on the design of laminated composite structures: Constant and variable stiffness design and topology optimization, Adv. Compos. Hybrid Mater. 1 (3) (2018) 460–477, http://dx.doi.org/10.1007/s42114-018-0032-7.

[3] C. Lopes, Z. Gürdal, P. Camanho, Variable-stiffness composite panels: Buckling and first-ply failure improvements over straight-fibre laminates, Comput. Struct. 86 (9) (2008) 897–907, http://dx.doi.org/10.1016/j.compstruc.2007.04.016.

[4] S. Khan, M.A. Nik, K. Fayazbakhsh, Z. Fawaz, Continuous curvilinear variable stiffness design for improved strength of a panel with a cutout, Mech. Adv. Mater. Struct. 29 (7) (2022) 975–983, http://dx.doi.org/10.1080/15376494.2020.1801914.

[5] M.A. Nik, K. Fayazbakhsh, S. Khan, Z. Fawaz, Strength evaluation of continuous curvilinear variable stiffness panels with circular cutouts under biaxial normal loading and off-design conditions, Mech. Adv. Mater. Struct. 29 (25) (2022) 3860–3870, http://dx.doi.org/10.1080/15376494.2021.1912441.

[6] S. Ilanko, L. Monterrubio, Y. Mochida, The Rayleigh-Ritz Method for Structural Analysis, John Wiley & Sons, Hoboken–USA, 2014.

[7] M.S. Qatu, A.W. Leissa, Free vibrations of completely free doubly curved laminated composite shallow shells, J. Sound Vib. 151 (1) (1991) 9–29, http://dx.doi.org/10.1016/0022-460X(91)90649-5.

[8] M.S. Qatu, A.W. Leissa, Natural frequencies for cantilevered doubly-curved laminated composite shallow shells, Compos. Struct. 17 (3) (1991) 227–255, http://dx.doi.org/10.1016/0263-8223(91)90053-2.

[9] P. Heyliger, A. Jilani, Free vibrations of laminated anisotropic cylindrical shells, J. Eng. Mech. 119 (5) (1993) 1062–1077, http://dx.doi.org/10.1061/(ASCE)0733-9399(1993)119:5(1062).

[10] L. Chun, K. Lam, Dynamic analysis of clamped laminated curved panels, Compos. Struct. 30 (4) (1995) 389–398, http://dx.doi.org/10.1016/0263-8223(94)00056-5.

[11] K. Lam, C. Loy, Influence of boundary conditions and fibre orientation on the natural frequencies of thin orthotropic laminated cylindrical shells, Compos. Struct. 31 (1) (1995) 21–30, http://dx.doi.org/10.1016/0263-8223(94)00054-9.

[12] K. Soldatos, A. Messina, Vibration studies of cross-ply laminated shear deformable circular cylinders on the basis of orthogonal polynomials, J. Sound Vib. 218 (2) (1998) 219–243, http://dx.doi.org/10.1006/jsvi.1998.1769.

[13] G. Jin, T. Ye, X. Ma, Y. Chen, Z. Su, X. Xie, A unified approach for the vibration analysis of moderately thick composite laminated cylindrical shells with arbitrary boundary conditions, Int. J. Mech. Sci. 75 (2013) 357–376, http://dx.doi.org/10.1016/j.ijmecsci.2013.08.003.

[14] G. Jin, T. Ye, X. Jia, S. Gao, A general Fourier solution for the vibration analysis of composite laminated structure elements of revolution with general elastic restraints, Compos. Struct. 109 (2014) 150–168, http://dx.doi.org/10.1016/j.compstruct.2013.10.052.

[15] C. Hwu, H. Hsu, Y. Lin, Free vibration of composite sandwich plates and cylindrical shells, Compos. Struct. 171 (2017) 528–537, http://dx.doi.org/10.1016/j.compstruct.2017.03.042.

[16] R. Vescovini, N. Fantuzzi, Free vibrations of conical shells via Ritz method, Int. J. Mech. Sci. 241 (2023) 107925, http://dx.doi.org/10.1016/j.ijmecsci.2022.107925.

[17] X. Zhao, T. Ng, K. Liew, Free vibration of two-side simply-supported laminated cylindrical panels via the mesh-free kp-Ritz method, Int. J. Mech. Sci. 46 (1) (2004) 123–142, http://dx.doi.org/10.1016/j.ijmecsci.2004.02.010.

[18] T. Ye, G. Jin, Z. Su, X. Jia, A unified Chebyshev–Ritz formulation for vibration analysis of composite laminated deep open shells with arbitrary boundary conditions, Arch. Appl. Mech. 84 (2014) 441–471, http://dx.doi.org/10.1007/s00419-013-0810-1.

[19] H. Li, F. Pang, C. Gao, R. Huo, A Jacobi-Ritz method for dynamic analysis of laminated composite shallow shells with general elastic restraints, Compos. Struct. 242 (2020) 112091, http://dx.doi.org/10.1016/j.compstruct.2020.112091.

[20] L. Kurpa, T. Shmatko, G. Timchenko, Free vibration analysis of laminated shallow shells with complex shape using the R-functions method, Compos. Struct. 93 (1) (2010) 225–233, http://dx.doi.org/10.1016/j.compstruct.2010.05.016.

[21] F. Pang, H. Li, H. Chen, Y. Shan, Free vibration analysis of combined composite laminated cylindrical and spherical shells with arbitrary boundary conditions, Mech. Adv. Mater. Struct. 28 (2) (2021) 182–199, http://dx.doi.org/10.1080/15376494.2018.1553258.

[22] Y. Zhang, D. Shi, Vibration analysis of laminated composite coupled double cylindrical shell-annular-rectangular plate system, Compos. Struct. 281 (2022) 115020, http://dx.doi.org/10.1016/j.compstruct.2021.115020.

[23] P. Zuo, X. Shi, R. Ge, J. Luo, Unified series solution for thermal vibration analysis of composite laminated joined conical-cylindrical shell with general boundary conditions, Thin-Walled Struct. 178 (2022) 109525, http://dx.doi.org/10.1016/j.tws.2022.109525.

[24] S. Arshad, M. Naeem, N. Sultana, Frequency analysis of functionally graded material cylindrical shells with various volume fraction laws, Proc. Inst. Mech. Eng. Part C: J. Mech. Eng. Sci. 221 (12) (2007) 1483–1495, http://dx.doi.org/10.1243/09544062JMES7.

[25] X. Zhao, Y. Lee, K.M. Liew, Thermoelastic and vibration analysis of functionally graded cylindrical shells, Int. J. Mech. Sci. 51 (9–10) (2009) 694–707, http://dx.doi.org/10.1016/j.ijmecsci.2009.08.001.

[26] J. Awrejcewicz, L. Kurpa, T. Shmatko, Linear and nonlinear free vibration analysis of laminated functionally graded shallow shells with complex plan form and different boundary conditions, Int. J. Non-Linear Mech. 107 (2018) 161–169, http://dx.doi.org/10.1016/j.ijnonlinmec.2018.08.013.

[27] G. Sciascia, V. Oliveri, A. Milazzo, P.M. Weaver, Ritz solution for transient analysis of variable-stiffness shell structures, AIAA J. 58 (4) (2020) 1796–1810, http://dx.doi.org/10.2514/1.J058686.

[28] G. Sciascia, V. Oliveri, P.M. Weaver, Eigenfrequencies of prestressed variable stiffness composite shells, Compos. Struct. 270 (2021) 114019, http://dx.doi.org/10.1016/j.compstruct.2021.114019.

[29] G. Sciascia, V. Oliveri, P.M. Weaver, Dynamic analysis of prestressed variable stiffness composite shell structures, Thin-Walled Struct. 175 (2022) 109193, http://dx.doi.org/10.1016/j.tws.2022.109193.

[30] K. Liew, S. Kitipornchai, A. Leung, C. Lim, Analysis of the free vibration of rectangular plates with central cut-outs using the discrete Ritz method, Int. J. Mech. Sci. 45 (5) (2003) 941–959, http://dx.doi.org/10.1016/S0020-7403(03)00109-7.

[31] Y. Song, Free vibration of arbitrarily shaped plates with complex cutouts, Thin-Walled Struct. 190 (2023) 110979, http://dx.doi.org/10.1016/j.tws.2023.110979.

[32] Z. Jing, L. Duan, Discrete Ritz method for buckling analysis of arbitrarily shaped plates with arbitrary cutouts, Thin-Walled Struct. 193 (2023) 111294, http://dx.doi.org/10.1016/j.tws.2023.111294.

[33] R. Vescovini, Ritz R-function method for the analysis of variable-stiffness plates, AIAA J. 61 (6) (2023) 2689–2701, http://dx.doi.org/10.2514/1.J062702.

[34] R. Vescovini, The R-functions combined with the Ritz method: An assessment on the integration schemes, Compos. Struct. 362 (2025) 119066, http://dx.doi.org/10.1016/j.compstruct.2025.119066.

[35] Q. Li, W. Huang, J. Sanchez, P. Wang, Q. Ding, J. Wang, Free vibration analysis of rectangular plate with cutouts under elastic boundary conditions in independent coordinate coupling method, CMES - Comput. Model. Eng. Sci. 134 (3) (2022) 2093–2121, http://dx.doi.org/10.32604/cmes.2022.021340.

[36] K. Tian, Y. Wang, B. Fang, D. Cao, K. Yu, X. Mei, A novel unified dynamical modeling of perforated plates based on negative mass equivalence, Mech. Syst. Signal Process. 232 (2025) 112723, http://dx.doi.org/10.1016/j.ymssp.2025.112723.

[37] A. Milazzo, G. Guarino, V. Gulizzi, Buckling and post-buckling of variable stiffness plates with cutouts by a single-domain Ritz method, Thin-Walled Struct. 182 (2023) 110282, http://dx.doi.org/10.1016/j.tws.2022.110282.

[38] Z. Jing, Variable stiffness discrete Ritz method for free vibration analysis of plates in arbitrary geometries, J. Sound Vib. 553 (2023) 117662, http://dx.doi.org/10.1016/j.jsv.2023.117662.

[39] D. Li, K. Chen, P. Hao, Z. Wu, Robust multi-curve trimming IGA method for layerwise composite plates with arbitrary cutouts, Compos. Struct. 360 (2025) 119043, http://dx.doi.org/10.1016/j.compstruct.2025.119043.

[40] M. Yao, S. Wang, Y. Niu, Q. Wu, C. Wang, Vibration characteristics of pre-twisted rotating Ti-SiC composite airfoil blade, Appl. Math. Model. 128 (2024) 392–409, http://dx.doi.org/10.1016/j.apm.2024.01.033.

[41] Y. Wan, S. Yang, R. An, Z. Wang, H. Yang, Free vibration of hinged FG-GPLRC magneto-electro-elastic variable-thickness folded trapezoidal sandwich panels, Acta Mech. Sin. 42 (4) (2026) 525120, http://dx.doi.org/10.1007/s10409-025-25120-x.

[42] Y. Liu, Z. Duan, C. Zhou, Y. Si, C. Guan, Y. Xiong, B. Xu, J. Yan, J. Zhu, Variable stiffness design optimization of fiber-reinforced composite laminates with regular and irregular holes considering fiber continuity for additive manufacturing, Chin. J. Aeronaut. 38 (3) (2025) 103317, http://dx.doi.org/10.1016/j.cja.2024.11.027.

[43] X. Sun, W. Sun, S. Lv, H. Luo, H. Zhang, Y. Zhang, Modeling and active control of C-shaped rods with variable-carbon-fiber-path, Int. J. Mech. Sci. 317 (2026) 111506, http://dx.doi.org/10.1016/j.ijmecsci.2026.111506.

[44] Y. Zhang, H. Zhang, H. Ma, W. Sun, D. Du, K. Xu, H. Li, Nonlinear vibration control of smart-composite-panels: Dynamic modeling and experimental testing, Int. J. Mech. Sci. 311 (2026) 111199, http://dx.doi.org/10.1016/j.ijmecsci.2026.111199.

[45] H. Zhang, Y. Zhang, W. Sun, H. Luo, H. Ma, K. Xu, Temperature-dependent identification and active vibration control under time-varying loads for composite laminates, Eur. J. Mech. A Solids 117 (2026) 106014, http://dx.doi.org/10.1016/j.euromechsol.2025.106014.

[46] P. Malekzadeh, F. Bahranifard, S. Ziaee, Three-dimensional free vibration analysis of functionally graded cylindrical panels with cut-out using Chebyshev–Ritz method, Compos. Struct. 105 (2013) 1–13, http://dx.doi.org/10.1016/j.compstruct.2013.05.005.

[47] S. Ren, P. Zhang, J. Li, Application of 2D modified Ritz technique to examine the effect of multiple cutouts on vibrational characteristics of composite conical panels based on an FG-X$^{\zeta}$ model, Eng. Anal. Bound. Elem. 179 (2025) 106413, http://dx.doi.org/10.1016/j.enganabound.2025.106413.

[48] D. Zhang, D. Li, J. Gao, Z. Wu, C. Jin, On the transient dynamics of FGM cylindrical panels with cutout under thermal shock employing 2D Chebyshev-based energy method, Thin-Walled Struct. 212 (2025) 113176, http://dx.doi.org/10.1016/j.tws.2025.113176.

[49] M. Lo Cascio, A. Milazzo, Free vibrations of composite cylindrical panels with cutouts of general shape, Aerotec. Missili Spaz. 105 (2) (2026) 125–138, http://dx.doi.org/10.1007/s42496-025-00266-4.

[50] S. Osher, R. Fedkiw, Level set methods and dynamic implicit surfaces, in: Applied Mathematical Sciences, vol. 153, Springer, New York, 2003, http://dx.doi.org/10.1007/b98879.

[51] E. Carrera, Theories and finite elements for multilayered, anisotropic, composite plates and shells, Arch. Comput. Methods Eng. 9 (2) (2002) 87–140, http://dx.doi.org/10.1007/BF02736649.

[52] J.N. Reddy, Mechanics of Laminated Composite Plates and Shells: Theory and Analysis, CRC Press, Boca Raton, 2003.

[53] E. Carrera, Theories and finite elements for multilayered plates and shells: A unified compact formulation with numerical assessment and benchmarking, Arch. Comput. Methods Eng. 10 (3) (2003) 215–296, http://dx.doi.org/10.1007/BF02736224.

[54] R. Khandan, S. Noroozi, P. Sewell, The development of laminated composite plate theories: A review, J. Mater. Sci. 47 (16) (2012) 5901–5910, http://dx.doi.org/10.1007/s10853-012-6329-y.

[55] P.G. Ciarlet, Mathematical elasticity, volume III: Theory of shells, in: Classics in Applied Mathematics, vol. 86, Society for Industrial and Applied Mathematics, 2022, http://dx.doi.org/10.1137/1.9781611976823.

[56] J.M. Whitney, N.J. Pagano, Shear deformation in heterogeneous anisotropic plates, J. Appl. Mech. 37 (4) (1970) 1031–1036, http://dx.doi.org/10.1115/1.3408654.

[57] N.J. Pagano, Exact solutions for rectangular bidirectional composites and sandwich plates, J. Compos. Mater. 4 (1) (1970) 20–34, http://dx.doi.org/10.1177/002199837000400102.

[58] Dassault Systèmes SIMULIA Corp., Abaqus theory guide, abaqus 6.14 documentation, 2014, Providence, RI, USA.

[59] A. Milazzo, Free vibrations analysis of cracked variable stiffness composite plates by the extended Ritz method, Mech. Adv. Mater. Struct. 30 (8) (2023) 1675–1691, http://dx.doi.org/10.1080/15376494.2022.2038742.

[60] P. Moreno-García, J.V.A. dos Santos, H. Lopes, A review and study on Ritz method admissible functions with emphasis on buckling and free vibration of isotropic and anisotropic beams and plates, Arch. Comput. Methods Eng. 25 (3) (2018) 785–815, http://dx.doi.org/10.1007/s11831-017-9214-7.

[61] A. Milazzo, V. Oliveri, Post-buckling analysis of cracked multilayered composite plates by pb-2 Rayleigh–Ritz method, Compos. Struct. 132 (2015) 75–86, http://dx.doi.org/10.1016/j.compstruct.2015.05.007.
[62] K. Liew, C. Wang, Pb-2 Rayleigh–Ritz method for general plate analysis, Eng. Struct. 15 (1) (1993) 55–60, http://dx.doi.org/10.1016/0141-0296(93)90017-X.
[63] K. Liew, C. Lim, L. Ong, Flexural vibration of doubly-tapered cylindrical shallow shells, Int. J. Mech. Sci. 36 (6) (1994) 547–565, http://dx.doi.org/10.1016/0020-7403(94)90031-0.
[64] R.I. Saye, High-order quadrature methods for implicitly defined surfaces and volumes in hyperrectangles, SIAM J. Sci. Comput. 37 (2) (2015) A993–A1019, http://dx.doi.org/10.1137/140966290.
[65] R.I. Saye, High-order quadrature on multi-component domains implicitly defined by multivariate polynomials, J. Comput. Phys. 448 (2022) 110720, http://dx.doi.org/10.1016/j.jcp.2021.110720.
[66] A. Talezadehlari, Free vibration analysis of perforated composite cylindrical shell and panel using multi-domain generalized differential quadrature (GDQ) method, Compos. Struct. 287 (2022) 115337, http://dx.doi.org/10.1016/j.compstruct.2022.115337.
[67] J. Fazilati, H. Ovesy, Finite strip dynamic instability analysis of perforated cylindrical shell panels, Compos. Struct. 94 (3) (2012) 1259–1264, http://dx.doi.org/10.1016/j.compstruct.2011.11.008.
[68] Z. Gürdal, B. Tatting, C. Wu, Variable stiffness composite panels: Effects of stiffness variation on the in-plane and buckling response, Compos. Part A: Appl. Sci. Manuf. 39 (5) (2008) 911–922, http://dx.doi.org/10.1016/j.compositesa.2007.11.015.
[69] V. Gulizzi, R. Saye, Modeling wave propagation in elastic solids via high-order accurate implicit-mesh discontinuous Galerkin methods, Comput. Methods Appl. Mech. Engrg. 395 (2022) 114971, http://dx.doi.org/10.1016/j.cma.2022.114971.